

Observability of Scattered-Light Echoes Around Variable Stars and Cataclysmic Events

Ben E. K. Sugerman

Department of Astronomy, Columbia University, New York, NY 10027

ben@astro.columbia.edu

ABSTRACT

Scattered light echoes from variable and cataclysmic stars offer one of the most effective means to probe the structure and composition of circumstellar and interstellar media. I build a simple model of light-echo surface brightness by considering the source spectrum, and the dust density, geometry, and scattering efficiency. I use this model to investigate whether echoes should be observable around short and long-period giants, cataclysmic variables, and supernovae. Only supernovae are expected to illuminate material on both circumstellar and interstellar scales. Giant and post-AGB stars (e.g. Cepheids and Miras) with high mass-loss rates can produce observable echoes within their circumstellar envelopes. Echoes from novae and dwarf novae are probably detectable only from nearby material, and only in unusually dense gas. I present characteristic exposure times to image such echoes over a wide range of wavelengths for ground-based and *Hubble Space Telescope* observations. I apply these results to analyze the dust properties of the recently-reported echoes around SN 1993J, finding the dust in M81 to have a grain-size distribution and chemical composition consistent with Galactic dust. Optimal observing strategies for echo detection are also discussed.

Subject headings: circumstellar matter — ISM: dust — stars: supernova (SN 1993J) — stars: variables — techniques: photometric

1. INTRODUCTION

Since Couderc (1939) proposed the theory of “auréoles lumineuses” to explain the otherwise superluminal sources surrounding Nova Persei 1901 (Ritchey 1901), scattered light echoes have offered one of the most effective means to probe circumstellar and interstellar structure. When the light pulse from some varying object is scattered by dust into the line of sight, an observable echo is produced, provided the pulse is sufficiently luminous and the dust sufficiently dense. An echo observed a given time after the pulse must lie on the locus of points equidistant in light travel from the source and observer, i.e. an ellipsoid with known foci. This simple geometry directly yields the three-dimensional position of an echo, uncertain only by the assumed distance to the source.

A great challenge to any observer is determining the distances of objects of interest along the line of sight. Whereas this normally requires a variety of positional and absorption-velocity information as well as a geometric model, the relative line-of-sight positions of light echoes are unambiguous, and can be determined with as little as a single image. Given a reliable distance determination to the source, the absolute position

of an echo and the precise three-dimensional structure of the surrounding dust are known. Conversely, light echoes can be employed to determine the distance to structures with independently-known geometry. Finally, as the spectrum of an echo is determined by the scattering properties of the dust, light echoes constrain the grain-size distribution, density, and composition of dust in the circumstellar (CSM) and interstellar medium (ISM), provided the input spectrum is known.

Light echoes have been considered in connection with gamma-ray bursts (Reichart 2001; Band & Hartmann 1992) and active galactic nuclei (de Diego et al. 1998), as distance indicators to galaxy clusters (Milgrom 1987; Katz 1987; Braun & Milgrom 1989), and for probing the baryon density of the universe with high- z sources (Sholomitskii 1997). If nearly-90° scattering occurs, the positions of maximally-polarized echoes yield geometric distance measurements to the echo source (Sparks 1994, 1996). The influence of echoes on the light curves of type II supernovae (SNe) has been discussed by e.g., Di Carlo et al. (2002), Roscherr & Schaefer (2000), Filippenko et al. (1995), Chugai (1992), and Mackey (1987). The detection of echoes has been investigated around SNe (Wright 1980; Chevalier 1986; Schaefer 1987a,b; Emmering & Chevalier 1989; Sparks 1994; Maslov 2000), novae (Gehrz 1988), and flaring stars (Argyle 1974; Bromley 1992; Gaidos 1994).

In spite of the wealth of information contained in echoes, light echo astronomy is still a nascent field. This is due in part to the relative difficulty of directly detecting them. Foremost, the brightest echo-producing objects (SNe) are also the rarest, and only a limited number of recent candidates are close enough to produce resolved echoes. Targeted searches around supernovae have been conducted by van den Bergh (1965a,b, 1966) and Boffi, Sparks, & Macchetto (1999). The latter search found 16 echo candidates out of a study of 65 historic SNe in 38 galaxies. Although no conclusive detections were made, echoes could be discovered around these candidates in follow-up observations. Novae are the next likely class of targets, and of the searches conducted by van den Bergh (1977) and Schaefer (1988), no echoes were detected. To date, echoes have actually been resolved around only a handful of objects. These include Nova (N) Per 1901 (Couderc 1939; Swenson 1948), N 1975 Cyg (Bode & Evans 1985), N V838 Mon (Munari et al. 2002; Bond et al. 2003), SN 1987A (see below), SN 1991T (Sparks 1994; Sparks et al. 1999), SN 1993J (Liu et al. 2002; Sugerman & Crots 2002), and SN 1998bu (Cappellaro et al. 2001). Variability in the circumstellar material around the Cepheid variable RS Pup (Havlen 1972; Mayes, Evans & Bode 1985) and the bipolar nebula OH 231.8+4.2 (the Rotten Egg nebula; Kastner et al. 1992) may also be interpreted as light echoes from the central variable star.

SN 1987A in the Large Magellanic Cloud (LMC) is the nearest known SN in the last 400 years. Due to its proximity, echoes around SN 1987A are the most widely discussed and extensively studied. It is beyond the scope of this article to give a full accounting of the references—there are at least 15 publications discussing the detection of echoes, not including regularly cited circulars and conference proceedings. These echoes have been used to map the surrounding circumstellar (Crots & Kunkel 1991; Crots, Kunkel & Heathcote 1995; Sugerman et al., in preparation) and interstellar (Xu, Crots & Kunkel 1994, 1995; Xu & Crots 1999) material, thereby probing the progenitor’s mass-loss history, its location within the LMC, as well as the structure and history of the associated stars and gas.

The low detection rate from intentional searches and small number of known echoes suggests that they are especially difficult to image, and may have discouraged interest in recent years. One may also speculate whether limitations in resolution and detector sensitivity, as well as unoptimized observing strategies, have contributed to these disappointing results and to the limited application of this technique. Under what circumstances can one hope to successfully image light echoes? Are there better observational techniques or more likely candidates to study? How can one maximize the information content of those observed?

In this article, I discuss the observability of scattered-light echoes around a variety of variable sources, and present an optimized observing method, which has already been proven successful. Formalisms for dust scattering are developed in §2, in which I build the components for predicting light-echo surface brightness in §3. Dust scattering properties are presented in §3.1, candidate variable stars for producing echoes in §3.2, and input constraints in §3.3. These components are used in §3.4 to compute the exposure times to image light echoes using ground-based telescopes, and the Advanced Camera for Surveys (ACS) and Space Telescope Imaging Spectrograph (STIS) aboard *Hubble Space Telescope* (*HST*). I apply the model to echoes recently discovered around SN 1993J in §4, and discuss an optimal observing strategy in the conclusions (§5).

2. FORMALISM

2.1. Light Echo Surface Brightness

Consider the geometry shown in Figure 1 (adapted from Xu et al. 1994), in which an object O at distance D from the observer emits a pulse of light of duration τ at time \tilde{t} . This light echoes off dust located at position \mathbf{r} from O , and reaches the observer at time t . This formalism was first developed to discuss light echoes from supernovae (Emmering & Chevalier 1988, 1989), for which \tilde{t} is measured from the time of explosion, and t is measured from the arrival of first visual light. For the more general case of any variable source, one can consider \tilde{t} to be the time at which maximum light was emitted from the source, and t is the time an echo is observed as measured from the arrival of maximum light.

Let us treat the dust as a thin planar sheet of thickness Δz ; this approximation is only for computational convenience but will not effect the generality of the result. The light scattered at \mathbf{r} lies on an ellipsoid with O and the observer at the foci. Since D is generally much greater than r , the echo depth z along the line-of-sight can be approximated by the parabola (Couderc 1939)

$$z = \frac{\rho^2}{2ct} - \frac{ct}{2} \quad (1)$$

where $\rho = r \sin \theta$ is the distance of the echo from the line-of-sight in the plane of the sky, and θ is the scattering angle. Since the light pulse and dust have finite widths, the echo will have a width $d\rho$ (§2.2).

The flux scattered off one dust grain of radius a at position \mathbf{r} is (Chevalier 1986; Emmering & Chevalier 1989)

$$dF_{\text{SC}}(\lambda, t, \mathbf{r}, a) = \frac{Q_{\text{SC}}(\lambda, a)\sigma_g L(\lambda, \tilde{t})\Phi(\mu, \lambda, a)}{16\pi^2 D^2 r^2} \quad (2)$$

where Q_{SC} is the grain scattering efficiency; $\sigma_g = \pi a^2$ is the grain cross section; $L(\lambda, \tilde{t})$ is the luminosity at λ and \tilde{t} ; and Φ is the scattering phase function for a given $\mu = \cos \theta = 1 - c(t - \tilde{t})/r$. I adopt the Henyey & Greenstein (1941) phase function

$$\Phi(\mu, \lambda, a) = \frac{1 - g^2(\lambda, a)}{[1 + g^2(\lambda, a) - 2g(\lambda, a)\mu]^{3/2}} \quad (3)$$

with $g(\lambda, a)$ measuring the degree of forward scattering for a given grain. The total flux F_{SC} from a single scattering is found by multiplying equation (2) by the dust density $n_d(\mathbf{r}, a)$ and integrating over the scattering volume and all grain sizes. I restrict this work to single-scattering events, and refer the reader to Chevalier (1986) for a discussion of multiple-scatterings, which are only of significance when the optical depth of the scattering material $\gtrsim 0.3$.

Proceeding as in Xu et al. (1994), for a thin sheet, changes in z can be ignored over the scattering volume. First, note that the flux $F(\lambda, \tilde{t}) = L(\lambda, \tilde{t})/4\pi D^2$, then

$$F_{\text{SC}}(\lambda, t) = \int Q_{\text{SC}}(\lambda, a) \sigma_g F(\lambda, \tilde{t}) \Phi(\mu, \lambda, a) \frac{n_d(\mathbf{r}, a)}{4\pi r^2} da d^3r. \quad (4)$$

Solving μ for \tilde{t} and substituting $r = \sqrt{\rho^2 + z^2}$,

$$\tilde{t} = t - \frac{\sqrt{\rho^2 + z^2}}{c} + \frac{z}{c}$$

and for a given time t

$$d\tilde{t} = -\frac{\rho d\rho}{cr}. \quad (5)$$

Consider the spatial part of equation (4) by transforming the integral to cylindrical polar coordinates

$$I = \int n_d(\mathbf{r}, a) \frac{F(\lambda, \tilde{t})}{4\pi r^2} \rho d\rho dz d\phi.$$

Substituting equation (5) and letting $dz = \Delta z$ and $F(\lambda) = \int F(\lambda, \tilde{t}) d\tilde{t}$,

$$I = \frac{c\Delta z}{4\pi r} F(\lambda) \int n_d(\mathbf{r}, a) d\phi.$$

Mathis, Rumpl, & Nordsieck (1977, hereafter MRN) found extinction of starlight through many lines of sight to be well reproduced if the distribution of dust grains in the ISM (for a given range of a) is given by

$$dn_{gr} = C n_{\text{H}} a^{-3.5} da \quad (6)$$

where $n_{gr}(a)$ is the number density of grains with radius $\leq a$, C is a normalization constant, and n_{H} is the number density of H nuclei. Since dn_{gr}/da and $n_d(\mathbf{r}, a)$ are both the number density of grains between $(a, a+da)$, equation (6) can be rewritten $n_d(\mathbf{r}, a) = n_{\text{H}}(\mathbf{r})f(a)$ where the exact form of $f(a)$ will be determined in §2.4.

Light echoes are observed as extended flux distributions, therefore we measure the surface brightness B_{SC} of scattered light. Noting that $F_{\text{SC}} = \int B_{\text{SC}} \rho \Delta\rho d\phi$ and $F_{\text{SC}}(\lambda, t) = \int F_{\text{SC}}(\lambda, t, \phi) d\phi$, equation (4) now becomes

$$B_{\text{SC}}(\lambda, t, \phi) = F(\lambda) n_{\text{H}}(\mathbf{r}) \frac{c\Delta z}{4\pi r \rho \Delta\rho} S(\lambda, \mu) \quad (7)$$

where the integrated scattering function

$$S(\lambda, \mu) = \int Q_{\text{SC}}(\lambda, a) \sigma_g \Phi(\mu, \lambda, a) f(a) da. \quad (8)$$

Since the observed flux $F(\lambda)$ and area element $\rho \Delta\rho$ diminish as D^{-2} , equation (7) for surface brightness is distance independent, as expected. If the light echo is close to the line of sight to O , the echo should suffer roughly the same extinction as the observed flux $F(\lambda)$, mitigated of course by the potentially higher dust density directly surrounding the echo location.

2.2. Light Echo Width

Since a light pulse has a finite duration τ , the observed light echo will have a width $d\rho_e$ resulting from the convolution of the dust thickness Δz and the pulse width

$$d\rho_t = \frac{cz + c^2t}{\rho}\tau. \quad (9)$$

This is shown schematically in Figure 2. Xu et al. (1995) approximate the echo paraboloids in the neighborhood of Δz by lines of slope $k = d\rho/dz$, and find the convolution of two gaussians of FWHM $\propto \Delta z$ and dr_t yields

$$\frac{1}{2d\rho_e^2} = \frac{1}{2d\rho_t^2} - \frac{(k/2d\rho_t^2)^2}{(k^2/2d\rho_t^2) + (1/2\Delta z^2)}$$

which simplifies to

$$\Delta z = \frac{\sqrt{d\rho_e^2 - d\rho_t^2}}{k}. \quad (10)$$

Using the light echo equation [eq. (1)] one finds

$$\frac{1}{k} = \frac{\rho}{ct}, \text{ and } d\rho_t = \left(\frac{\rho}{2t} + \frac{c^2t}{2\rho}\right)\tau$$

with which equation (10), solved for $\Delta\rho = d\rho_e$, becomes

$$\Delta\rho = \sqrt{\left(\frac{\rho}{2t} + \frac{c^2t}{2\rho}\right)^2 \tau^2 + \left(\frac{ct}{\rho}\right)^2 \Delta z^2}. \quad (11)$$

Since z and $r = \sqrt{\rho^2 + z^2}$ are both functions of (ρ, t) , the geometric factors in equation (7)

$$G(\rho, t, \tau, \Delta z) = \frac{c\Delta z}{4\pi r \rho \Delta\rho} \quad (12)$$

and μ can be written in terms of observables (ρ, t, τ) with Δz the only unknown. This allows an echo to be specified in terms of the dust structure (Δz) rather than its observed width ($\Delta\rho$). The geometric factors G and θ are shown in figure 3. In discussing the geometry it is often easier to use units of years and light-years, since $c = 1$.

2.3. Time-Integrated Flux

To compute the surface brightness of an echo, one must know the time-integrated monochromatic flux $F(\lambda)$. If a homogenous time-series of spectra exist for a given object, one simply integrates them over time, provided they have sufficient spectral coverage for the wavelength range in question. For this paper, I wish to explore the observability of echoes around a variety of objects, and over a large wavelength range (1000–11000Å). Time-series of spectra are available for many (but not all) objects of interest, and the wavelength coverage is highly inhomogenous, thus such an approach for determining $F(\lambda)$ is not ideal. Rather, I propose a method by which a single spectrum can be used to approximate the time-integrated flux. This has the added bonus that it defines the value of τ [eq. (12)] in a consistent manner.

Although a light pulse has finite duration, its flux varies substantially during τ . Furthermore, determination of the exact value of τ is ambiguous – some commonly-used values are the time for flux to vary

by two or three magnitudes, or the “effective width” $\int F(t)dt/F(t_{max})$. Since fainter fluxes contribute less to light echo signal, a compromise must be reached between inclusion of a reasonable portion of the light curve (i.e. the wings), and exclusion of faint fluxes whose contributions to an echo are negligible compared to the peak flux. Sample light curves of composite Type II-P SNe (Doggett & Branch 1985) and the Mira star χ Cyg are shown in Figure 4. These curves can be approximated in the neighborhood of their maxima by parabolae in magnitude space. A parabola with vertex $(0, \log f_0)$ and passing through $(t', \log f_1)$ can be written

$$\log f(t) = \log f_0 - \frac{t^2}{t'^2}L \quad (13)$$

where $L = (\log f_0 - \log f_1)$. The area A under the curve between $\pm t$ is found by integrating $f(t)$:

$$A(t) = \frac{t' f_0 \sqrt{\pi}}{\sqrt{L \ln 10}} \operatorname{erf}(t\sqrt{L \ln 10}/t'). \quad (14)$$

The error function erf approaches unity if the operand is $\gtrsim 1.4$, that is if $t > t_c = 1.4t'/\sqrt{L \ln 10}$. Let t_n be the time required for the flux to drop by n magnitudes, or equivalently, for $\log[f(t)]$ to drop by $0.4n$. Applying this constraint to equation (13), one finds $t_n = t'\sqrt{0.4n/L}$. Equation (14) is roughly constant for $t_n > t_c$ or $n \gtrsim 2.1$. Thus, a reasonable value of τ is $2t_2$, i.e. the time required for the flux to rise then diminish by 2 magnitudes. At $\tau = 2t_2$, equation (14) reduces to

$$A(t_2) = 0.95 \frac{f_0 t'}{\sqrt{L}} \sqrt{\frac{\pi}{\ln 10}} \approx 1.11 \frac{f_0 t'}{\sqrt{L}}. \quad (15)$$

By choosing to construct the parabola with $t' = t_2$, $\sqrt{L} = \sqrt{0.8}$ and $A(t_2) = 1.25f_0t_2$. With this, an approximation for the time-integrated monochromatic flux $F(\lambda)$ in equation (7) can be expressed by $F(\lambda) = 1.25F(\lambda, t_{max})t_2$, where t_{max} is the time of maximum light.

How does this prescription for measuring τ compare with other methods? To address this, I have calculated a number of diagnostic widths of the mean B light curves for type Ia, II-P and II-L supernovae from Doggett & Branch (1985), which the authors provide in an interpolated tabular form. The results are given in Table 1. The left columns give the values of τ for the five methods noted below. The right columns show how much of the total flux of the light curve is included in this measurement of τ . The methods are: (1) the effective width reported by Sparks (1994); (2) the effective width I calculate integrated from maximum light; (3) the effective width I calculate by integrating the whole light curve; (4) the time for the light curve to actually rise and fall by 2 mags from maximum light; (5) twice the time for the light curve to fall 2 mags from maximum light. There is a large dispersion among the different methods, demonstrating the ambiguity of this measurement. The effective width measured from maximum light is roughly half the value to rise/fall by 2 mags, showing that despite the dispersion among methods, they are qualitatively consistent. Aside from the type II-L curve, whose integrated flux saturates very quickly, the effective-width measurements (methods 1–3) exclude roughly one-quarter of the energy released in the outburst.

To some extent, it is up to the individual to select which prescription for τ is preferred. In the context of this paper, the t_2 formulation presented above gives an estimate not only of the width of the light pulse, which is needed in G [eq. (12)], but also of the time-integrated flux $F(\lambda)$ that enters equation (7). For the purposes of exploring a general parameter space, I will use equation (15), and caution the reader that integrated fluxes may be in error by 10–25%. In practice, the spectral energy distribution of a variable object changes over τ , which this prescription for $F(\lambda)$ does not take into account. Generating an empirical time-integrated spectrum is the obvious method of choice, provided (as noted above) one has sufficient spectral

and temporal coverage. In §4, I discuss the error associated with this approximation applied to SN 1993J, and present an easily-implemented method of correction.

2.4. Dust Properties

In their classic analysis, MRN found that a mixture of carbonaceous and silicate grains following a density distribution given by equation (6) adequately modeled observed starlight extinction. Draine & Lee (1984) and Laor & Draine (1993) calculated the dielectric functions for graphite and “astronomical silicate,” from which they calculated the dust properties (Q_{SC} , Q_{ABS} , and g) using the dipole approximation (valid for $a/\lambda \lesssim 0.1$) and Mie theory (van de Hulst 1957). Q_{ABS} is the absorption efficiency, relevant when considering IR emission or optical extinction. Weingartner & Draine (2001, hereafter WD01) have corrected an anomolous feature in the silicate dielectric function, while Li & Draine (2001) have included the effects of small PAH molecules in carbonaceous grains. Values of $Q_{\text{SC}}(\lambda, a)$ and $g(\lambda, a)$ are shown¹ in Figure 5, for both carbonaceous and silicate dust over a variety of grain radii and wavelengths.

WD01 have constructed a new dust-grain density distribution $f(a)$ fit to observed interstellar extinction. I refer the reader to their paper for the actual functional form, but note that it contains a smooth cutoff for large and small grain sizes and allows the slope $d \ln n_{gr}/d \ln a$ to vary, unlike the fixed slope of equation (6). I have adopted their preferred Milky Way dust model for {case A, $R_V = 3.1$, and $b_C = 6 \times 10^{-5}$ }, shown in Figure 6, which works well at fitting both optical extinction and infrared dust emission (Li & Draine 2001) in diffuse clouds. For comparison, more reddened sightlines are well fit by the {case A, $R_V = 5.5$, $b_C = 3 \times 10^{-5}$ } density model, also shown in Figure 6. The reddening ratio $R_V = A_V/E(B-V)$ (Cardelli, Clayton & Mathis 1989), and b_C is the total C abundance per H nucleus. I caution that these particular density distributions are not unique, and WD01 discuss a range of parameter space that fit the observed galactic optical extinction (roughly) equally well. Furthermore, extragalactic dust densities need not follow that of our galaxy; the authors find a different dust distribution for the LMC extinction, for example. Uncertainty in the density distribution is to be expected, since e.g. (as noted by WD01) the dielectric functions are not precise, dust grains have poorly-understood surface monolayers, and grains are nonspheroidal. As such, predictions based on the adopted interstellar dust grain distribution should be taken with a proverbial salt grain.

2.5. Exposure Time Calculation

Since the aim of this paper is to discuss light echo observability, I briefly review the calculation of exposure times for a generic telescope, instrument, observing conditions and input spectrum. The signal-to-noise (S/N) ratio for an exposure time t is given by the CCD equation (Howell 2000)

$$S/N = C_{obj}t / [(C_{obj} + C_{sky} + C_{bg})t + n_{DC}(t + t_{RO}) + n_{RD}^2 + G^2\sigma_f^2]^{1/2} \quad (16)$$

where t_{RO} is the read-out time of the detector; G is the CCD gain [$e^- \text{ DN}^{-1}$]; 1 DN is one “data number,” or count (also known as ADU); n_{DC} is the dark current [$e^- \text{ s}^{-1} \text{ pix}^{-1}$]; n_{RD} is the read noise [e^-]; σ_f is the digitization noise of the digital-to-analog converter [DN] and is ~ 0.3 (Howell 2000); and C indicates the count rate [$e^- \text{ s}^{-1} \text{ pix}^{-1}$], with C_{obj} for the object observed, C_{sky} is that of the sky, and C_{bg} is the

¹Tabulated values are available at <http://www.astro.princeton.edu/~draine/dust/dust.diel.html>

background, e.g. nebulosity or galaxy surface brightness. Dark current, read time, gain and read noise are properties of the detector. For a desired S/N it suffices to solve the quadratic in equation (16) for t .

The count rates are computed from the sensitivity of the system (as clearly explained in Leitherer et al. 2001), which gives the counts per unit wavelength resulting from unit incident flux. The sensitivity is calculated as (the effective area of the telescope at λ) divided by (the energy per photon at λ). Let us define $T_X(\lambda)$ to be the total throughput of the observational configuration X (e.g. telescope, filter, detector) at wavelength λ , then sensitivity is $T_X(\lambda)A\lambda/hc$ where A is the area of the primary mirror, and hc is Planck’s constant times the speed of light. It follows that for an object with surface brightness $B(\lambda)$, the count rate

$$C = \frac{A}{hc} m_X^2 10^{-0.4A_X} \int B(\lambda) T_X(\lambda) \lambda d\lambda \quad (17)$$

where m_X is the platescale [arcsec pix⁻¹] and A_X is the extinction in filter X . For a 2.4-m telescope (typical of a moderate-sized ground-based observatory or *HST*) $A/hc = 2.3 \times 10^{12}$ cm² erg⁻¹ Å⁻¹. Throughputs for ACS, STIS and Johnson filters, including *HST* optics, are taken from *symphot*. Although a ground-based telescope will not have the same throughput as *HST*, this approximation should be sufficient. For *HST*, detector characteristics and “typical” sky brightnesses ($m_V = 22.7$ mag arcsec⁻¹, including zodiacal and geocoronal light) are taken from the Instrument Handbooks (Pavlovsky et al 2002; Leitherer et al. 2001). For a generic 2.4-m ground-based telescope, I adopt sky brightness estimates for 3 days after new moon from Walker (1987), and use characteristics typical of a SITE 2048 × 2048-pixel thinned and backside-illuminated CCD with 0.24μm pixels, with platescale computed at f/15.

For ground-based observations, I consider Johnson and Cousins filters between U and I . STIS has three cameras of interest: the optical long-pass F28x50LP filter and the two MAMA detectors (near and far UV). For ACS, I consider the optical Wide Field Camera (WFC), the optical and near-UV High-Resolution Camera (HRC), and the UV Solar-Blind Camera (SBC). Characteristics for all filters and detectors used in this work are listed in Tables 2 and 3, respectively.

2.6. Extinction

As noted in §2.1, an echo and source should suffer the same extinction, provided their angular separation is small. Using the observed (i.e. not extinction corrected) source spectrum for $F(\lambda)$, extinction need not enter equations (7) or (17). Since in this work I will often use template spectra (§3.2), extinction must be included in surface-brightness calculations. Furthermore, it is important to know how much extinction is caused by the echoing dust, in order to rule out unreasonable regions of the parameter space (i.e. density or composition).

The power per unit area of an electromagnetic wave traveling a distance L through dust of density n_d will be attenuated by a factor $\exp(-n_d L C_{\text{EXT}})$ (Draine & Lee 1984). The factor C_{EXT} is the extinction scattering cross section, defined as the sum of the scattering and absorption cross sections C_{SC} and C_{ABS} . Since the cross section is related to efficiency by $Q = C/\sigma_g$, the extinction (in magnitudes) can be calculated by

$$A_\lambda = (2.5 \log e) N_H \int (Q_{\text{SC}} + Q_{\text{ABS}}) \sigma_g f(a) da \quad (18)$$

where $N_H = n_H L$ is the column density of hydrogen nuclei along the optical path.

I have integrated equation (18) using the dust density, scattering and absorption properties discussed in §2.4. Integration was performed using the extended Simpson’s method (Press et al. 1992), with values for Q

and g interpolated logarithmically in λ and a . Figure 7 shows the resulting extinction for $R_V = 3.1$ and 5.5 for Galactic dust, as well as the individual contributions from silicate and carbonaceous dust. For comparison, I also show the extinction curves from Cardelli et al. (1989) in each panel. As these are reported as A_λ/A_V , I have normalized them to the computed total extinction at 5495\AA (the value at which $A_\lambda/A_V = 1$). The fit is very reasonable for both reddening parameters. From these curves, the value of A_X in equation (17) can be calculated, given either an estimate for A_V or N_H .

2.7. Non-Planar Dust Distributions

Figure 8 shows schematic situations typical of a CSE around a mass-losing star. Mass-loss produces an r^{-2} (gas) density profile, shown here as a greyscale gradient. The inner and outer radii are chosen such that R_{in} designates the radius at which dust condenses in the wind, and R_{out} is a matter boundary, such as when the wind density reaches that of the ISM. As discussed in §2.2, one will observe an echo from all the material located between the echo parabolae marking the beginning (t_1) and end (t_2) of the light pulse or the star’s high-flux state. An echo in a CSE differs from the simple case explored in the previous subsections since density now varies as a function of scattering position. Some variable stars have periods larger than the light-crossing time of the envelope, thus the envelope material swept up between the echoes at t_1 and t_2 will be substantial, as shown in panel (a). In this “thick echo” regime, one may consider the light echoing from a single column of width $\Delta\rho$ of this envelope. Although the overall geometry is not planar, one can apply the planar approximation by integrating thin planar contributions along this column. If the period of variation is smaller than the envelope size, one may consider the “thin echo” situation depicted in panel (b), where a single sight line looks through many nested parabolae (for clarity I have only drawn 12 echoes, although 39 fit into this geometry). The contributions from all such echoes must be included.

If the envelope has high optical depth, the single scattering approximation is no longer valid. For the purposes of this work, single scattering will be sufficient, since $A_V < 1$ in most dust geometries (§3.3.4). A more thorough analysis of multiple scatterings should be investigated for cases when $A_V \gtrsim 0.3$, however this first approximation will serve as a guide to whether such echoes will be observable at all.

3. THE LIGHT ECHO MODEL

3.1. Dust Scattering

Computation of the integrated scattering function $S(\lambda, \mu)$ is a straightforward integral over grain sizes, using equations (3), (8) and the dust-density models from WD01. Selected results are plotted in Figure 9, showing the dependency of $S(\lambda, \mu)$ on density distribution model, grain size range, composition, and scattering angle. Columns show a given scattering angle θ with varying grain-size range, and rows show a fixed size range for varying θ . Changes along columns are due strictly to the limits of integration for S , while changes along rows are the result of variations in the scattering phase function Φ . The three size-range distributions are denoted “S” (small, $a = 5 \times 10^{-4} - 0.01\mu\text{m}$), “M” (mid-sized, $a = 0.01 - 0.1\mu\text{m}$) and “G” (Galactic range, $a = 5 \times 10^{-4} - 1.0\mu\text{m}$). “Galactic” dust is the full density distribution adopted by Weingartner & Draine (2001).

Scattering for grains with $a < 0.1\lambda/2\pi$ occurs within the Rayleigh limit, for which $S \propto \lambda^{-4}$. This behavior is clearly seen in the top row in Figure 9 and in the second row, for $\lambda \gtrsim 5000\text{\AA}$. For the smallest

silicate grains, $S \propto \lambda^{-4.3}$, while $S \propto \lambda^{-4.2}$ for carbonaceous dust with $\lambda > 3000\text{\AA}$. This “super-Rayleighian” behavior reflects the dielectric function and resonance effects (B. Draine 2002, private communication). As the maximum grain-size increases, scattering efficiency increasingly deviates from λ^{-4} behavior, but UV scattering is generally more efficient than optical.

Of particular interest are the scattering peaks seen in the UV (1000–2500Å). The presence of the strong 1500Å carbonaceous peak/dip in the bottom row (type G dust) demonstrates the tendency of large dust to predominantly forward scatter near this wavelength. This conclusion is borne out by observing how the scattering function changes with $\mu = \cos \theta$. Regardless of the adopted form for the scattering phase function, Φ should be larger (smaller) for scattering toward (away from) the observer. For equation (3), as $\mu \rightarrow \pm 1$, $\Phi \rightarrow (1 \pm g)/(1 \mp g)^2$, thus as the forward scattering efficiency g approaches 100%, Φ grows large for $\theta = 0$ and small for $\theta = 180^\circ$. The degree of forward scatter $g \gtrsim 0.8$ for larger grains ($a \gtrsim 0.1\mu\text{m}$) at 1500Å, but $g \lesssim 0.04$ for grains smaller than $0.01\mu\text{m}$. Large grains tend to forward-scatter UV light, while small grains scatter more isotropically. Thus we expect a UV bump near 1500Å for $\theta \sim 0$ large-grain scattering, and a dip for $\theta \rightarrow 180^\circ$, as observed in the bottom row of Figure 9.

Maxima in S near 1000Å and 2175Å in carbonaceous grains are clear when the large-grain $\lambda = 1500\text{\AA}$ resonance is not present, i.e. for the smallest grain sizes and for $\theta \rightarrow 180^\circ$. These two features demonstrate the high scattering efficiency Q_{SC} of dust at short wavelengths. The 2175Å bump is a known interstellar scattering and extinction band (Stecher 1965; Stecher & Donn 1965), which WD01 attribute to PAHs. The 1000Å maximum is an artifact of the wavelength range plotted, and S continues to increase for shorter wavelengths (there is another bump around 800Å). Large silicate grains also show a bump around 2000Å, the origin of which is unclear.

Figure 9 suggests that a great deal about dust can be learned from carefully-planned observations of light echoes. The actual light echo flux will be a function of the total dust density, grain size distribution, and the relative population of carbonaceous-to-silicate grains, geometry and light-pulse characteristics notwithstanding. Since we generally know the latter two, echo colors and magnitudes should constrain the dust properties. Assume for now that the density distribution function is known, and only the grain-size limits, density and composition are not. The observed echo spectrum will be a product of the dust scattering $S(\lambda, \mu)$ and the pulse spectrum $F(\lambda)$ (§3.2), from which object-specific echo models can be created.

Echo geometry fixes Φ , indicating on which column in Figure 9 the total dust scattering efficiency must lie, while the dust model can be chosen from R_V , as determined from stellar spectrophotometry. Optical colors alone may distinguish the largest from the smallest dust grains (since smaller grains at longer wavelengths follow the Rayleigh scattering relationship), however since the dust number density (expressed here in terms of hydrogen density) will likely be unknown, brightnesses themselves will not conclusively distinguish between various particle-size scenarios. Fortunately, blue to UV fluxes are a strong measure of dust size, and UV-to-optical colors should lift the small-particle degeneracy. Furthermore, aptly chosen wavebands can distinguish emission from the various scattering maxima, which are sensitive to dust composition. For example, the STIS MAMA far and near UV filters have average wavelengths and FWHM of (1381Å,324Å) and (2310Å,1237Å), respectively, with only mild overlap at 1500Å. The question remains whether echoes at these wavelengths are easily observable. Finally, it is important to note that spectroscopy, even in low resolution but covering a wide wavelength range, is likely the best observational strategy for studying dust properties through light echoes.

3.2. Variable Objects: Selection and Spectra

To predict the brightness of echoes from different sources, it is first necessary to select candidate objects to study. The primary selection criterion is that the object vary in brightness by a significant amount. Without variability, any scattering material will appear as a reflection nebula rather than as echoes, and no 3-D information can be gleaned. A second criterion is that the duration of variability is short compared to the light-travel time across at least one dimension of the scattering medium. A burst of duration 100 days can not give any spatial information about a dust shell of radius 1 light day, but can still map the dust in a thin but extended dust sheet since the sheet’s dimensions are wider on the plane of the sky than the pulse width. I list in Table 4 classes of variable objects that change in brightness by $\Delta V \gtrsim 2$ mag. For easy comparison, the data are also shown in graphical form in Figure 10. Four broad categories are present: supernovae, cataclysmic variables (CVs), pulsating giants and eruptive stars.

To model echo brightness, and to discuss the relative brightness between different wavebands, it is necessary to provide a realistic representation of the object’s emission spectrum in the factor $F(\lambda)$ in equation (7). Selected representational spectra for the first three categories are plotted in Figure 11, and discussed below. Each spectrum has been normalized to a distance of 1 pc. This slightly-unconventional normalization has been chosen to balance the conversion from physical area $(\rho\Delta\rho)^{-1}$ in G (§2.2) to angular area. Since these will represent the flux at maximum brightness, I will refer to these as $F(\lambda, t_{max})$.

Supernovae: Immediately following core collapse, type II supernova shock breakout is brightest at shortest wavelengths. The short-lived but intense pulse of UV emission will photoionize any surrounding circumstellar material, and likely evaporate the smaller, nearest ($d \ll 1$ pc) dust grains (see Emmering & Chevalier 1989), however larger and more distant grains should survive. As shown in §3.1, dust scattering is most efficient in the UV for most echo geometries, making dust echoes of the UV pulse an attractive observational target. The later-time spectrum is dominated by optical emission from cooling lines and radioactive decay, and provides the longer-duration optical pulse that is reflected in optical light echoes. To model echoes from SNe, I use synthetic spectra of SN 1987A from day 1 after core collapse (when the SN was UV bright; Figure 11a), and day 58 after core collapse (nearing the maximum optical light; Figure 11b), generated with the *Phoenix* stellar and planetary atmosphere code (E. Baron 2002, private communication). Both spectra were normalized using a LMC distance of 50 kpc. A *Phoenix* synthetic spectrum of a Type Ia event 25 days after explosion (not shown) has stronger flux than SN 1987A (a Type II SN) at day 58, and while the microscopic features are different, the overall spectrum is similar. I will therefore use the Type II spectrum for echo calculations, with a caution to the reader that type Ia events are 1–2 mag brighter.

CVs: Within this category are classical, recurrent and dwarf novae, and symbiotic stars, together spanning up to 10 mag between the brightest and faintest outbursts, with such mechanisms as thermonuclear runaway on an accreting white dwarf to accretion disk instabilities. To model echoes from classical novae, I use synthetic spectra of a nova outburst during the fireball (Figure 11c) and constant luminosity (Figure 11d) phases, again generated with the *Phoenix* code (P. Hauschildt 2002, private communication). Both have been normalized to Nova LMC 1991 (Schwarz et al. 2001) assuming an LMC distance of 50 kpc. Recurrent novae (including U Sco and RS Oph) should be adequately modeled as classical novae with slightly less flux. Dwarf novae (DNe) come in a variety of flavors: U Gem, Z Cam, SS Cyg and SU Uma DNe have amplitudes of 2–6 magnitudes during normal outbursts, while TOADs – SU Uma and WZ Sge categories – can have outburst amplitudes of 6–10 mag (Howell, Szkody, & Cannizzo 1995). As DNe are abundant, quasi-periodic, and can be bright, they may provide a generous target list of echo candidates.

DNe occur from instabilities in binary-star accretion disks. The theoretical spectrum of an infinitely-

large, steady-state accretion disk is given by $F_\lambda \propto \lambda^{-7/3}$ (Lynden-Bell 1969), however since the disk has a discrete inner edge (the accreting white dwarf) this law is more reasonably written $F_\lambda \propto \lambda^{-2.1}$ (J. Patterson 2002, private communication). A normalized (to 1pc) spectrum is easily generated from this law using SS Cyg: $F(\lambda) = 1.4\lambda^{-2.1}$ where λ is in \AA (Polidan & Holberg 1984; Harrison et al. 1999).

Pulsating Giants and Supergiants: Pulsating giant stars include (but are not limited to) long-period variables (LPVs) such as post-ABG thermal-pulsating carbon stars and Miras, G–K type supergiant RV Tauri stars, and F–K type Cepheids. Figure 11e shows the spectrum of the M7III star SW Vir, available in the Bruzual-Persson-Gunn-Stryker (BPGS) spectrophotometry atlas within *synphot*. Itself a semi-irregular variable, SW Vir has a spectral type similar to the prototypical Mira *o* Cet. This spectrum has been normalized using the star’s Hipparcos parallax of 7 mas (Perryman et al. 1997). As expected of a cool giant, the energy distribution is predominantly red.

A Cepheid has a type F1b spectrum during maximum brightness. Many such stars exist in the Jacoby-Hunter-Christian (JHC) spectrophotometric atlas within *synphot*, but only between 3500–7400 \AA . To generate a Cepheid-like spectrum with the full wavelength coverage needed, I scaled the F0IV spectrum of ξ Ser (from the BPGS catalog) to the F6Ib spectrum of HD 8992 (from the JHC catalog), having first normalized HD 8992 to a Hipparcos distance of 0.82 mas, and corrected ξ Ser for an extinction of $A_V = 0.015$ (listed in the file header). Figure 11f shows the resulting spectrum.

Eruptive Stars: Many stars in this class do not satisfy the required criteria, such as R Coronae Borealis, which fades rather than brightens; UV Ceti stars, which have pulsation durations of seconds to minutes; or Wolf Rayet stars, which only vary by $\Delta V \sim 0.1$ mag. However, the S Doradus class is a high-luminosity blue star, typically surrounded by diffuse nebulosity or expanding envelopes. η Car is a famous member of this class, but with a period of over 5 years. I note this class for completeness, and although echoes might be observable in the extended envelopes, I will not make predictions for these stars.

3.3. Observability of Light Echoes – Constraints

Prior to integrating equation (7), we must specify the echo geometries and dust densities for each candidate object. Once specified, this integral yields the source count rate to be inserted into the CCD equation [eq. (16)], along with the appropriate values from Tables 2 and 3 and an estimate of the background C_{bg} . An echo is deemed “observable” if it can be detected at a given signal-to-noise level in a “reasonable” exposure time. In the following sections, I discuss estimates for exposure time, dust density and geometry, extinction, and sources of background flux.

3.3.1. Exposure Time

Since light echoes are transient objects, they are effectively detected by PSF-matched difference imaging, in which one matches the PSFs between two images using a variety of techniques prior to subtracting them. This offers a minimally-invasive method for removing all sources of constant flux, with only sources of variable brightness remaining. The differencing technique of Tomaney & Crotts (1996) has been shown by Sugerman & Crotts (2002, hereafter SC02) to be quite effective at detecting light echoes in *HST* imaging, as well as in e.g. the monitoring of hot spots in SNR 1987A (Lawrence et al. 2000; Sugerman et al. 2002), detection of variable stars in globular clusters (Uglesich et al. 1999), and the M31 microlensing project (Crotts 1992;

Uglesich 2002).

Direct photometric techniques (such as aperture photometry or even PSF-fitting and removal) can only remove resolved point sources, but have difficulty identifying faint surface-brightness features within the fluctuations of an unresolved background component. In differencing two images, these unresolved sources are removed, leaving (in principle) only statistical noise. Even though this noise increases by $\sqrt{2}$, the detection threshold (i.e. required S/N) for an echo decreases notably in a difference image, since we are looking for coherent signal over a large, and now statistical-noise dominated, area. A well-resolved echo need only be detected at $S/N = 2-3$ (per pixel) to appear unambiguously above the difference-image background. I will adopt a per-pixel $S/N = 3$ as the required detection threshold.

The assessment of a “reasonable” exposure time is subjective, but not without practical constraints. A reasonable series of *HST* observations would image in 3–5 filters within perhaps double the number of orbits. With 50–70 minutes per orbit, a 30–90 minute exposure seems a reasonable maximal exposure time. Ground-based observations are much more flexible, and I will consider a six-hour (total) exposure time in any given filter as a representational (but by no means fixed) upper limit.

3.3.2. Gas and Dust Density

For all model predictions, I will assume dust follows the type G (or Galactic) dust distribution (§3.1). To calculate the dust density, it is first necessary to specify n_H , the density of hydrogen nuclei, which normalizes dn_{gr}/da to give the dust density within interstellar gas. The use of this normalization factor depends on the assumption of a constant gas-to-dust ratio in the ISM, however this same ratio may be unreasonable for circumstellar environments. The dust distribution integrates to yield a gas-to-dust ratio of 124, and total number densities (per material) of $n_C = 6.0 \times 10^{-7}n_H$ and $n_{Si} = 3.5 \times 10^{-8}n_H$ for carbonaceous and silicate dust (respectively) with $R_V = 3.1$, while the $R_V = 5.5$ distribution gives $n_C = 3.0 \times 10^{-7}n_H$ and $n_{Si} = 4.5 \times 10^{-10}n_H$. For a given dust composition ($n_d = an_C + bn_{Si}$), the above densities can be used to rescale n_H to the appropriate dust content within any environment.

Comparison of these dust densities with previously-reported values for the ISM will be problematic, since the WD01 density profile favors a large number of extremely small grains. Small particles are inefficient scatterers at optical wavelengths: $Q_{SC} = 10^{-10} - 10^{-8}$ for particles with $a = 3 \times 10^{-4} - 10^{-3}\mu\text{m}$, while $Q_{SC} > 10^{-5}$ for $a > 5 \times 10^{-3}\mu\text{m}$ (Fig. 5). These grains contribute little to optical scattering, and have been ignored in previous density distributions. Their effect on the total density is easily understood by considering the MRN distribution in equation (6), which integrates to yield $n_{gr} \propto (a_{min}^{-2.5})$ for $a_{min} \ll a_{max}$. This behavior strongly biases the density by their presence, yielding values much larger than generally quoted. For a meaningful comparison with previous work, I have integrated the WD01 distribution over the size limits given by MRN: $0.005 \leq a_C \leq 0.25$ and $0.01 \leq a_{Si} \leq 0.25$. With these limits, the total number densities for $R_V = 3.1$ are $n_C = 7.6 \times 10^{-11}n_H$ and $n_{Si} = 2.3 \times 10^{-11}n_H$, while for $R_V = 5.5$, $n_C = 4.1 \times 10^{-11}n_H$ and $n_{Si} = 2.8 \times 10^{-12}n_H$.

Interstellar Dust: Following the multi-stage ISM model of McKee & Ostriker (1977), the majority of interstellar gas will be in either the hot ($n_d \gtrsim 10^{-3}$) or warm ($n_d \sim 0.1 - 1$) states. Were we to regularly observe echoes from this ambient-density medium, one would expect to see a diffuse halo around echoing objects, rather than discrete arcs and rings. This suggests that we detect most light echoes from only the denser regions of the ISM, however molecular clouds ($n_H \gtrsim 1000$, $r \sim 50\text{pc}$) have sufficiently high extinctions ($A_V \gtrsim 5$) that echoes should not be observed. Rather, echoes likely originate from HI clouds with $n_H \sim 10$,

which have sheet-like features and extinctions $A_V < 1$ (R. Chevalier 2003, Private Communication).

Mass-losing giants: Post-AGB stars have mass-loss rates of 10^{-8} to $10^{-4} M_\odot \text{ yr}^{-1}$, yielding circumstellar density profiles $n_d = Kr^{-2}$ (where K is a constant of proportionality), and with dust condensing within the outflow as near as $8R_*$, where R_* is the stellar radius $\sim 3 \times 10^{13}$ cm (Habing 1996). Justtanont, Skinner, & Tielens (1994) find gas-to-dust ratios of ~ 200 for oxygen-rich red-giant winds, which implies that a factor of $0.6n_H$ can be used to predict the dust density. Vassiliadis & Wood (1993) find for Miras a mass-loss scaling relation $\log \dot{M} = -11.4 + 0.0123P(\text{days})$, yielding $\dot{M} \sim 10^{-9} M_\odot \text{ yr}^{-1}$ for a 200 day Mira. The equation of continuity predicts that the constant $K = 3 \times 10^{43} \dot{M}/v_\infty$ where \dot{M} is in $M_\odot \text{ yr}^{-1}$ and v_∞ is the gas terminal velocity in km s^{-1} , typically 5–25 km s^{-1} for AGB stars, and 30 km s^{-1} for cool giants (Lamers & Cassinelli 1999). As such, $K \sim 3 \times 10^{33} \text{ cm}^{-1}$ for 200-day Miras. Cepheids have mass-loss rates between 10^{-10} to $10^{-6} M_\odot \text{ yr}^{-1}$ (Deasy 1988). While most cepheids shed mass at the slower rate, high mass-loss examples are known, such as RS Pup, whose mass-loss is estimated by Deasy (1988) to be $\sim 10^{-6}$. At this rate, the density law will have $K = 10^{36} \text{ cm}^{-1}$, while at $\dot{M} = 10^{-9}$, $K = 10^{33} \text{ cm}^{-1}$.

CVs: Dust can condense in a stellar wind once the equilibrium temperature of the gas is less than $\sim 1500\text{K}$, which occurs (Lamers & Cassinelli 1999) at a radius

$$r_c \simeq \frac{R_*}{2} \left(\frac{T_*}{T_d} \right)^{\frac{4+p}{2}} \quad (19)$$

where $p \sim 1$ for silicate and $p \sim 2$ for carbonaceous dust. For a dust condensation temperature $T_d \sim 1000\text{K}$, $p = 1.5$, a white dwarf/accretion disk effective temperature of $(4 - 10) \times 10^4 \text{ K}$, and an inner radius $R_* = 10^9 \text{ cm}$, this yields $r_c = (1 - 16) \times 10^{13} \text{ cm}$. UV resonance-line profiles from DNe imply mass loss rates of $\dot{M} = 10^{-9} M_\odot \text{ yr}^{-1}$ (Vitello & Shlosman 1993) with terminal velocities in the range of 3000–5000 km s^{-1} (Warner 1995). For the smaller-velocity limit, the continuity equation gives $K = 10^{31} \text{ cm}^{-1}$.

3.3.3. Dust geometry

The geometric parameters entering G [eq. (12)] are listed in Table 5 and discussed below.

Mass-Losing Giant Stars: Post-AGB and Mira stars (and realistically, most stars late in their lifetimes, such as $\eta \text{ Car}$, SN 1987A) have complex stellar outflows, often bipolar or asymmetric, and are of critical interest as progenitors of an increasingly complicated taxonomy of planetary nebulae (as demonstrated in Kastner, Soker & Rappaport 2000). Although the scattering geometry is not planar in dusty envelopes (as in Figure 1), as discussed in §2.7, we can still apply the planar approximation. As shown in Figure 8, the echo will occur between two parabolae at t_1 and t_2 , separated in time by τ . The choice of geometric parameters representing typical echoes is somewhat arbitrary. Below, I discuss the geometries I will test.

The prototypical Mira $\chi \text{ Cyg}$ has an inferred CO shell extending to $\sim 3 \times 10^{16} \text{ cm}$ (Jorissen & Knapp 1998), while the post-AGB carbon star V Hya shows evidence of bipolar outflows at radii of $\sim 1.5 \times 10^{16} \text{ cm}$ (Sugerman, Sahai & Hinkle 1996). As the pulsation periods are large compared to this size, I use the thick-echo approximation (§2.7). As suggested by the aforementioned stars, one radius to test is $3 \times 10^{16} \text{ cm}$, as well as 10^{17} cm . For both cases, I choose t_1 so an echo passes through r with $\theta = 30^\circ$. I take the period to be 200 days, $\tau=50$ days, and $\dot{M} = 10^{-9} M_\odot \text{ yr}^{-1}$. This is shown schematically in Figure 8a.

For Cepheids, I use an envelope geometry suggested by RS Pup. Variations in light intensity in the surrounding nebula were interpreted by Havlen (1972) as arising from shells of reflecting material spaced

between inner and outer radii of roughly 5×10^{17} and 2.3×10^{18} cm. This inner radius is roughly $\frac{1}{2}$ ly, much longer than any Cepheid pulsation rate, thus the thin-echo approximation applies. I consider the innermost echo to be located within a shell with radii given above, with t_1 such that the inner echo passes through R_{out} at $\rho = R_{in}$. This is shown to scale in Figure 8b. I test two cases: that for the high mass-loss rate of RS Pup, and a more typical Cepheid mass-loss rate of $10^{-9} M_{\odot} \text{ yr}^{-1}$.

Classical Novae: The first nova outburst will eject $10^{-4} - 10^{-5} M_{\odot}$ of material at hundreds to thousands of km s^{-1} (Bode & Evans 1989), expanding into the ISM in a manner analogous to that of a SN, the physics of which is well studied (e.g. Chevalier 1974). Indeed, this is believed to be the case for Nova Per 1901 (Seaquist et al. 1989). Light echoes from this event may highlight the CSE into which the ejecta will travel, thereby allowing us to better understand (in the future) how the ensuing nebula formed, as well as the mass outflow characteristics of the star pre-nova (i.e. in its quiescent binary period). Recurrent novae may echo off their swept-up ejecta shells, providing direct testing of predictions for these lower-energy ejecta. Furthermore, such echoes will constrain the recurrence time of novae, a quantity which remains only speculative. Both types of bright novae may illuminate undisturbed ISM material as well.

Nova Per 1901 was a bright ($\Delta V \sim 13$) classical nova, and notably it is the first object around which light echoes were detected. Seaquist et al. (1989) have analyzed the archival imaging of GK Per following its 1901 outburst, concluding that the echoes analyzed on day 210 by Couderc (1939) were from a plane of dust with $r = 1.4$ pc at nearest approach, and with thickness $\Delta z \sim 0.15$ pc. It is unclear if this was true interstellar material, or a previously swept-up shell of circumstellar material. I will consider a sheet of dust with these characteristics, as well as dust with (somewhat arbitrary) thicknesses of $\Delta z = 5$ ly at $z = 50$, and $\Delta z = 25$ ly at $z = 250$ ly.

Dwarf novae: Being much less energetic in their outbursts than classical novae, DNe may not evacuate their circumstellar material in the same way, and hence may illuminate their quiescent stellar mass loss. GK Per currently has DN outbursts, the brighter of which might echo off the swept up nova shell. Of particular interest is the geometry of outflows near the white dwarf. While most accretion systems drive narrowly-collimated jets (e.g. T Tauri stars, X-ray binaries, quasars), non-magnetic CVs show evidence for mass loss with large inferred opening angles (Knigge & Drew 1997), suggesting these are accretion systems in which jets are absent (Knigge & Livio 1998). I consider a TOAD nova echoing from circumstellar ($r = 0.025$ ly) and interstellar ($r = 25$ ly) dust, as well as a dust sheet similar to that just discussed from N Per 1901. As the thickness of dust within the DN wind is uncertain (due in part to the unknown orientation of the outflow axis) I will arbitrarily take Δz to be a light day.

Supernovae: Supernovae offer the means to illuminate the most distant material, thereby probing the largest portions of the ISM. Unfortunately, the observability of resolved echoes around SNe is limited by the low frequency of nearby events. As in the previously-discussed objects, echoes from circumstellar and interstellar dust offer invaluable information on the progenitor’s evolution and the surrounding ISM. In particular, echoes can probe multiple stages of progenitor mass loss as imprinted in “snow-plow” contact-discontinuities with the ISM (e.g., Crotts & Kunkel 1991, for SN 1987A). I study six possible dust geometries, two each from circumstellar, contact discontinuity, and interstellar regions, using geometric parameters similar to echoes observed around SN 1987A (Crotts et al. 1995; Xu et al. 1995).

3.3.4. Extinction

To account for interstellar extinction from the light echo to Earth, I use the extinction curve in Figure 7, which relates A_λ in terms of A_V . However, the choice of this parameter depends on the particular line of sight and the distance of the echo from Earth. Rather than consider the myriad sightlines of objects, I adopt $A_V = 0.25$, with the caveat that predictions for specific objects may require different extinction values.

Mass-Losing Giants: Consider the trajectory of photons from the central star to the point of scattering and subsequently out of the CSE. In the single-scattering limit, light is extinguished along both paths. An estimate of the extinction can be calculated using the extinction curve in Figure 7, from which $A_V = 3 \times 10^{-22} N_H$ for $R_V = 3.1$ and a gas-to-dust ratio of 200. The column density is simply the integral of density along the photon path $N_H = \int n(r) dl$. For a radial path between R_{in} and r , $N_H = K(R_{in}^{-1} - r^{-1})$. For a line-of-sight path between θ and $\theta_{out} = \sin^{-1}(\rho/R_{out})$, and with impact parameter ρ , $N_H = K(\theta - \theta_{out})/\rho$. K is the constant of proportionality in the r^{-2} density profile, discussed in §3.3.2, and is in the range $10^{33} - 10^{37} \text{ cm}^{-1}$.

The extinction in the radial trajectory from the star to the echo is very sensitive to the radius at which dust condenses within the CSE, since $N_H \propto R_{in}^{-1}$ (provided $r \gg R_{in}$). Using equation (19), and assuming $p = 1.5$ and that dust condenses around $T_d = 1000\text{K}$, $r_c = 10R_*$ for a 3000K AGB star. This is consistent with Habing (1996), who notes that for outflows from cool stars, dust condenses at a radius of $8R_*$. At this radius and with $\dot{M} = 10^{-9} M_\odot \text{ yr}^{-1}$, the maximal extinction is $A_V = 0.004$. For a smaller and hotter Cepheid such as RS Pup ($R_* \sim 185R_\odot$, $T_* \sim 5600\text{K}$; Deasy 1988), dust will condense around $60R_*$. With $\dot{M} = 3 \times 10^{-6} M_\odot \text{ yr}^{-1}$, $A_V \leq 0.4$, while for $\dot{M} = 10^{-9} M_\odot \text{ yr}^{-1}$, $A_V \leq 4 \times 10^{-4}$. By and large, the single-scattering approximation is valid for CSE echoes since the extinction is < 1 .

3.3.5. Background Flux

Mass-Losing Giants: The entire column of gas containing the echo (delimited with vertical lines) in Figure 8 will scatter starlight into the line of sight, contributing the dominant source of background light when the echo is imaged at time t . Calculation of this background requires an additional integral of equation (7) over the line-of-sight trajectory, also corrected for internal extinction. Consider panel (a) at a later time t' , say when the variable star is passing through minimum and the echo has left the shell. The echo in the column shown will only be detectable in a difference image if the total flux at t (echo and background) can be distinguished from the total flux at t' (background only). In the thin-echo approximation, there will never be a time when the CSE does not have an echo in it. Instead, one must ask whether the entire column of echoes at t is detectable against a background of echoes at a later time t' , such as half a period later. To implement this, I will use the column of flux at t' as the background flux in equation (16).

CVs and SNe: I assume that any CSEs these stars might have are optically thin compared to the mass-losing giants, and that extinction effects can be ignored. In this case, sources of background flux will be the star's quiescent light scattered off the surrounding dust, and any unresolved background surface-brightness component. The former is estimated as the echo flux diminished by ΔV for the object (as colors change during outburst, this is only an approximation). For the latter, I adopt a background component of $\mu_V = 18.5 \text{ mag arcsec}^{-1}$, which is typical of extragalactic disks, in particular the disk of M81 at the location of SN 1993J (Sugerman & Crots 2002). To scale this to other wavelengths, I use the template spectrum of an Sb galaxy from the Kinney-Calzetti catalog within *synphot*, normalized so the flux in V is unity.

3.4. Observability of Light Echoes – Predictions

Armed with scattering efficiencies S (§3.1), echo constraints (§3.3), and light-pulse spectra (§3.2), calculating the expected count rate C_{obj} of light echoes is a simple integration of equation (17) over wavelength for a given set of filters and detectors. The resulting exposure times are plotted in Figures 12–16 for a supernova, classical nova, TOAD nova, Mira, and Cepheid (respectively). From §3.3.1, “reasonable” exposure times are of order 1h for *HST* and 6h for ground-based imaging, corresponding to $\log t$ of 3.5 and 4.3, respectively. These have been marked in each figure.

3.4.1. Supernovae

Optical echoes from supernovae are known to be observable, and Figure 12 confirms this for a wide variety of echo geometries. Interstellar UV echoes ought to be very difficult to observe, as most lie above the exposure-time limits. This is unfortunate since UV echoes are the most effective at constraining the grain-size distribution. Since the input spectrum was for SN 1987A 1 day after shock breakout, the UV pulse is likely stronger than the adopted spectrum at short wavelengths. This would decrease the exposure times in the UV, perhaps making the near-UV echoes observable with long exposures.

3.4.2. Novae

Light echoes from three novae have already been observed (§1), however targeted searches have had difficulty making positive detections (van den Bergh 1977; Schaefer 1988). We therefore expect for these echoes to be fainter and require longer exposure times. Figure 13a shows that circumstellar echoes may be observable across most optical wavebands, but even the closer of the two interstellar echoes [panels (b-c)] requires long integration times. If interstellar echoes are to be observed, one is restricted to high dust densities, energetic outbursts, and small depths ($z \lesssim 100$ ly).

3.4.3. Dwarf Novae

Exposure times for TOAD novae are shown in Figure 14. Circumstellar echoes from accretion-driven winds [panel (a)] may be observable in optical wavebands for the brightest TOAD novae, depending on the density and thickness of the gas. If such echoes are detected, either in ground-based imaging or with *HST*, we can place much better constraints on the outflow properties. Panel (b) is calculated for the snow-plow of the wind into the ISM, and unless the gas densities are unusually high, such echoes, as well as interstellar echoes [panel (c)] will most likely not be detected. Given that TOADs are roughly 6 mag brighter than ordinary DNe, it is highly unlikely that DNe will produce detectable echoes as well.

3.4.4. Miras

Figure 15 shows the exposure times for imaging an echo within the CSE of a Mira. These cool supergiants have extremely red spectra and little UV flux, thus we expect their exposure times for the shortest wavebands to be quite long. As this is indeed the case, filters shorter than Johnson *U* are not plotted in this figure. The

results are encouraging in that a variety of echoes should be observable. It is of interest however that while the template spectrum (Figure 11f) has little flux blueward of 6000\AA , echoes from the B and V wavelengths may still be observable. This is fortunate since, as shown in §3.1, larger wavelength coverage of an echo yields greater constraints on the scattering dust. As a matter of practical importance, these echoes will be close (in angular separation) from the central source, which itself is highly luminous and will thus create a confusion region. If one can obscure the bright central source (i.e. with a coronagraph), light echoes can be observed within the CSE, provided the dust grain sizes are sufficiently large.

3.4.5. Cepheids

Figure 16 shows the exposure times to image variations in nested, thin echoes within the circumstellar envelope of a bright Cepheid. As in the previous figure, filters shorter than Johnson U are not plotted. For two epochs separated by half a pulsation period, such variations should just be detectable for the high mass-loss case [panel (a)] with large platescale detectors. They are effectively undetectable for the lower mass-loss rates. Modulations in the total echo signal at a given sightline through the CSE will vary with the same frequency as the pulsating star, which implies that a difference of two images separated by half a period will appear as a series of concentric bright and dark rings. This is seen by Sparks (1997) in optical images of RS Pup, suggestive of the nested-echo interpretation. Of course, an additional challenge will be disentangling the contribution of each nested echo.

3.5. Caveats

These results only delineate whether or not echo flux is distinguishable from typical, smooth background noise under limited conditions. A second criterium for observability is for the echo to be unambiguously distinguishable from background sources. Although in this work I advocate the use of PSF-matched difference imaging, I must caution that this technique is optimal only within inherent observational constraints, which I briefly enumerate below. (1) To correctly compute the Fourier transform of a PSF, it must have sufficient spatial sampling, which translates in practice to a $\text{FWHM} \gtrsim 2.2$ pixels. Most *HST* and some good-seeing ground-based observations (with large detector platescales) produce stellar profiles narrower than this limit, necessitating image degradation and introducing subtraction errors. (2) Depending on the CCD used, a star that is bright enough to fill a pixel beyond its linear regime can leave subtraction residuals at the core, while saturated stars will create residuals within 1–3 FWHM radii. (3) Since point-sources have much higher flux than the background, the increased Poisson noise will leave subtraction residuals in the core of any bright (but linear) star. (4) Bright point-sources in *HST* observations suffer from large-radius diffraction patterns, particularly at short wavelengths. In practice, these PSF-wings are never well subtracted by PSF-matching (due to the much lower signal-to-noise in these regions), and PSF-subtraction (i.e. with Tiny Tim model PSFs) is only moderately effective at removing this signal at large radii. (5) Many sources of noise can take on stellar or extended profiles during data reduction. Hot pixels and cosmic rays mimic undersampled stellar profiles following geometric transformation. (6) Charge-transfer efficiency anomalies create extended tails around bright stars. (7) Ghosts from bright stars reflecting off optical surfaces produce a wide variety of extended structure (e.g. WFPC2 ISR 95-06), including echo-like arcs.

Given these considerations, an echo should have a sufficiently large angular separation from its source to not lie in the confusion region of its PSF, i.e. within a few FWHM. Stars on STIS images, for example,

have $\text{FWHM} \sim 0''.1$, while ground-based imaging can achieve $0''.5$ seeing under extremely-good conditions. Let us consider radial separations larger than $0''.5$ to be safe from source confusion. Most echoes imaged to date have been rings or arcs of large angular extent ($\gtrsim 20^\circ$ in position angle). To reliably distinguish an echo from a subtraction residual or anomalous background noise, it should be sufficiently well-resolved to have an equally-large angular size. At $0''.5$ separation, an echo of arclength 30° will span roughly 6 pixels. Echoes of larger arclength should appear as coherent signal over the background and through any other stellar PSFs. The chance of observing of an echo is maximized if we require the angular separation between the echo and source to be greater than this lower limit of $0''.5$, which in turn provides a maximum distance at which the echo source can be located. This parameter has been listed in the final column of Table 5, and the value can be easily scaled for any other telescope and detector combinations.

The above arguments imply that the results presented in Figures 12–16 only serve to suggest which echoes *could* be detected. The calculated exposure times do not account for the various noise sources discussed, largely because they are much more difficult to characterize in general terms. Stellar subtraction residuals are the dominant source of noise, and their presence is a sensitive function of the wavelength observed as well as the density and distribution of stars in the field. The readership should fold in these considerations with respect to their target fields. Also, I have attempted to generate generic dust geometries for producing echoes, but the actual geometry and density can vary substantially from target to target. Finally, extremely short exposure times ($t_{exp} \sim 1$ sec) suggest an echo should be easily detected with an integration of typical duration (30–600s), while very long exposure times imply an echo will only be observable under very extenuating circumstances.

4. Applications

The primary motivation for building the light echo model presented in this paper was to quantify the observability of echoes around a variety of variable objects. Once echoes are detected however, this same model is critical in interpreting the data. Given an object’s object spectrum, either template or observed, one may construct a series of expected spectral distributions against which the actual echoes may be compared, to constrain the dust size distribution, composition and gas density. Similarly, if echoes are not detected around a given object, this model provides limiting constraints on the above parameters.

As an application of the techniques described in this work, I discuss the light echoes recently discovered around SN 1993J (Liu et al. 2002, SC02). Both groups report the detection of an echo south-west from the SN in WFPC2 imaging taken 8.2 years after core collapse (UT 19 April 1993; Benson et al. 1994), at a radial distance from the SN of roughly $1''.9$ and 120° in angular extent (denoted SW770 in SC02). From the echo equation [eq. (1)], this corresponds to a depth $z = 770$ ly from the SN, assuming a SN distance of 3.63 Mpc (Freedman et al. 1994). Using PSF-subtraction and PSF-matched difference imaging, SC02 identify two additional echo candidates: one located $1''.15$ north-east of the SN (denoted NE260), and a marginal detection of SW770 in images taken only 1.8 years after core collapse. The direct and PSF-matched difference images in F555W from SC02 are shown in Figures 17a and 17d, respectively. The advantage of difference imaging is made most apparent by a comparison of the noise reported by both groups in the F555W image. Liu et al. (2002) report a null detection at the position of NE260 with measured noise of 9.2 DN pix^{-1} , while SC02 measure a flux of 4 DN pix^{-1} with a background noise of only 1.5 DN pix^{-1} . The reason the noise differs between the two groups is addressed in §3.3.1: difference-imaging removes surface brightness fluctuations (from non-variable, unresolved stars, nebulosity, etc.) that contribute to the “background” of direct photometric techniques.

Having constructed a dust model from the the MRN grain-size distribution and the scattering properties of Draine & Lee (1984), Liu et al. (2002) present four model fits to their measured surface brightness of SW770 in F450W, F555W and F814W. Each model overpredicts the blue photometry at $\sim 2\sigma$, while only the pure-graphite model is consistent in the red. The poor fitting in the blue is most likely a result of their overly-dim measurement of SW770 in F450W. If one shifts the surface brightness in this filter to within the errors of the F555W data (SC02 find roughly equal F450W and F555W fluxes), these models are reasonable fits. Of note, they suggest these echoes are explained by dust with density $n_d \sim 7 \times 10^{-10}$ grains cm^{-3} embedded within gas of density $n_H \sim 3 \text{ cm}^{-3}$. How does the echo model from this work compare?

In Figure 18, I present model surface brightnesses for a variety of compositions and grain-size distributions discussed in this paper. In estimating the exposure times in §3.4, I made the assumption that the peak-flux spectrum of an object is a reasonable representation of the spectrum over t_2 , however for detailed modeling of echoes, this may introduce systematic errors. Integrated fluxes for SN 1993J exist only in ground-based filters (Benson et al. 1994; Richmond et al. 1994), however the echoes are measured in WFPC2 filters, which differ enough from their Johnson and Cousins counterparts that it may be unwise to directly intercompare them. I generate the time-integrated flux $F(\lambda)$ as follows.

Predictions are based on an average of observed spectra from 17 and 24 days after core collapse (Barbon et al. 1995, acquired from the SUSPECT supernova spectrum archive). Although taken roughly 3 days before and after maximum light, these particular spectra have wider wavelength coverage than that taken at maximum light. This spectrum ends around 9500\AA but the F814W WFPC2 filter extends to 11000\AA . As an approximate solution, I fill in this gap with the Type Ia maximum-light template spectrum, renormalized so the transition around 9500\AA is smooth. I caution the reader that this will introduce additional error into F814W predictions. This composite spectrum is integrated over the B , V , and I_C response curves, and t_2 is chosen to match the total ground-based fluence. With $t_2 = 40$ days, this spectrum reproduces the V fluence to better than 1%; note that 40 d is also the effective width ($\int F(t)dt/F(t_{max})$) of the SN light curve reported in SC02. The fluences in B and I_C are correct using this value of t_2 if the B flux is corrected by 0.94, and the I_C by 0.77, when integrating over wavelength in equation (17). These corrections are applied when computing the predicted WFPC2 fluxes.

Predicted surface brightnesses are compared to the observed values reported by SC02 for two positions along SW770: the central region around PA 220, and the extremal PA 270, at which the echo becomes unusually blue. In each panel, the gas density n_H has been individually calculated to produce the observed F555W measurement for each echo location. I consider pure silicate dust, pure carbonaceous dust, and a Galactic composition (equal mixture of both as given by Weingartner & Draine 2001), for the type S, M and G grain-size distributions with $R_V = 3.1$ and 5.5. Toward SN 1993J, Richmond et al. (1994) and Prabhu et al. (1995) find $E(B - V) = 0.08 - 0.32$ mag, while values for A_V range from 0.25–1.0 mag (Richmond et al. 1994; Lewis et al. 1994), yielding R_V as high as 7.3. For completeness, I also present the model results for the MRN size distribution.

As the model predictions in F814W are the least accurate, these data should carry the least weight when considering the goodness of fit. A comparison of the fit to F450W and F555W only shows that all three MRN models, and the Type G $R_V = 3.1$ models for pure silicate and Galactic dust, are the best fits. It is of little surprise that the MRN fits closely mimic the Type G $R_V = 3.1$ fits, since both density models were tuned to fit Galactic dust. Including the F814W data as a constraint suggests the need for a highly carbonaceous dust distribution.

We can also judge the goodness of fit by the implied extinction of the predicted dust distributions. With

$\tau = 0.11$ y, $\rho = 108$ ly, and $\Delta\rho = 11.5$ ly, equation (11) suggests the echoing material has a line of sight depth of $\Delta z = 47$ ly. Using the extinction data in Figure 7, Type G silicate and carbonaceous dust with $n_{\text{H}} = 10 \text{ cm}^{-3}$ will produce $A_V=0.40$ and 0.33 (respectively) for $R_V = 3.1$, and 0.49 and 0.20 for $R_V = 5.5$. Thus, Galactic dust will produce respective extinctions of $A_V=0.73$ and 0.69 for $R_V = 3.1$ and 5.5 . Since extinction scales linearly with hydrogen density, purely carbonaceous type G dust would cause roughly 2 mags of visual extinction. As also noted by Liu et al. (2002), this is an unlikely fit as such optically thick dust would obscure background star and galactic light as well. Similarly, the type M and S dust models would require unreasonably-high extinctions, and can be safely discarded. With $n_{\text{H}} = 10 \text{ cm}^{-3}$, and including roughly 0.25 mag of Galactic extinction, the Type G Galactic dust models predict $A_V \sim 1$, consistent with the extinction found near the SN by Richmond et al. (1994).

It is of little surprise that the above results are inconclusive, since there are many more degrees of freedom than constraints. This stresses the need for broad waveband coverage in the interpretation of echo signal. In particular, follow-up observations of SN 1993J should integrate longer and include R and U -band imaging. Despite the shortcomings of this dataset, it illustrates a number of important points.

Foremost, the observed surface brightnesses are well reproduced by the light echo model. The dust in the disk of M81 (in the vicinity of SN 1993J) appears to follow a grain-size distribution and have a chemical composition similar to that of Galactic dust. Gas densities of order 10 cm^{-3} are required to produce the observed echoes, which for $R_V = 3.1$ translates into dust densities of roughly 10^{-9} cm^{-3} , in agreement with that found by Liu et al. (2002). The color shift in PA between the two echo locations discussed is easily explained by a small change in the density of the echoing material. This may be a simpler hypothesis than speculating the presence of large compositional gradients of (mostly) pure silicate to pure carbonaceous dust. Furthermore, we may also propose an explanation for the absence of the detected echo at other PAs. The noise reported by SC02 for their F555W difference image is 1 DN pix^{-1} for a scaled exposure time² of 953 s. This corresponds to a 1σ detection limit of $25 \text{ mag arcsec}^{-2}$, or a hydrogen density of about 2 cm^{-3} . By no means conclusive, this is suggestive that a simple density gradient in the cloud or sheet containing the echoing dust can adequately explain the observations. This substructure may be better understood through repeated observations and with a more extensive wavelength coverage.

5. Conclusions

In this paper, I have presented a model for calculating the brightness of a scattered light echo. I find that echoes from supernovae should be the most easily observed, while cataclysmic variables may only produce detectable echoes in the innermost circumstellar regions. Post-AGB and Cepheid variables should also produce observable echo signal, although the interpretation of such data will be technically challenging.

These results help explain why previous targeted searches have had such difficulty in directly detecting light echoes. For novae, it is fairly likely that echoes were too faint to be observed. For supernovae, the case is not as clear. In itself, a genuine null result is interesting, since it places reasonably strong limits on the dust density distribution along the line of sight. More likely is that many echoes were lost within the surface brightness fluctuations of background unresolved starlight (for SNe in external galaxies) or even

²Difference images are empirically scaled to stellar flux of the reference image prior to subtraction. In this case, the input was a 2000 sec F555W WF4 integration taken 2001 June 4, and the reference was a 900 sec F555W PC integration taken 1995 January 31. A scaling of 953 sec includes the effect of resampling the PC image to WF4 resolution.

moderately-crowded stellar fields, typical of observations close to the Galactic plane.

Consider the effect of simply increasing the platescale of the detector in otherwise ideal observing conditions. As a single pixel images a larger portion of the sky, a light echo will fall on fewer pixels, becoming increasingly confused with the background. Although the echo flux per pixel increases (aiding detection), so does the background, and point sources become increasingly crowded. The echo SW770 around SN 1993J (§4, Fig. 17a), happens to be clearly visible above the background in direct F555W imaging ($m \simeq 0''.1 \text{ pix}^{-1}$), but is completely lost when the resolution is degraded by a factor of four, as shown in Figure 17c. A platescale of $0''.4 \text{ pix}^{-1}$ is not uncommon by ground-based standards, and for such an echo, direct photometric techniques would likely have yielded a null detection. Unlike SW770, echo NE260 is only visible in the difference image, since in the direct data, its flux is indistinguishable from background fluctuations. Even with the high resolution of *HST*, direct imaging will miss echo signal.

Now consider the same exercise using PSF-matched difference imaging. Since all sources of constant brightness will be removed, the echo still stands out notably from the background when degraded images are differenced (Fig. 17e–f). Still at issue is resolving the echo from its source, which we see can not be done for NE260 at $0''.4 \text{ pix}^{-1}$. A successful series of observations must therefore have sufficient resolution to separate the echo from its (variable) source, although this does not forcedly require the use of *HST*. In the case of SN 1987A, ground-based imaging was more than sufficient to image interstellar echoes (Xu et al. 1995). For ideal difference-image quality, effort should be taken to ensure a stable and well-focused PSF, with individual exposures timed to avoid bright star saturation, and total exposure time sufficient to minimize background noise.

It is noteworthy that well-resolved echoes in ground-based observing can be just as easily imaged as from space. This is mainly due to the platescale factor of m_X^2 in equation (17). A ground-based integration will have > 9 times the flux per pixel compared to the ACS WFC camera, which more than compensates for the increased sky background over vacuum observations. Additionally, ground-based observations generally have a wider field-of-view, thereby maximizing the volume probed for light echoes. However, increased platescale corresponds to diminished angular resolution, requiring the echo source to be either closer to earth or more distant on the sky. Also, seeing greatly diminishes spatial resolution, thereby washing out any substructure within the echo. The observer must decide which consideration is more important.

The question of *when* to observe an echo remains. Unfortunately, there is no concrete prescription. The best image to difference against is one in which there are no echoes, which implies either observing the object prior to a burst, or median-combining a long baseline of imaging to attempt to average out any echo signal. Immediately following e.g. a nova outburst, the central source is too bright for deep imaging, yet it is during this time that echoes sweep through the innermost circumstellar material. Coronagraphy is likely the best options at these early times. Long after an outburst, the most easily observed echoes will come from forward-scattering geometries, which for large t imply large depth z and angular separation ρ . However, since echo brightness decreases with increasing dust distance and scattering angle, and suffers increasing extinction with total optical path length, echoes will become fainter as time progresses. While only a small effect for recently discovered SNe, this must be considered for Galactic SNe such as SN 1006. Echoes from historic outbursts must be evaluated on a per-case basis with the model presented here. Outside these two extremes, imaging should be taken in regular intervals of roughly twice the outburst duration, to minimize the overlap of a single echo off the same patch dust in both epochs. With such considerations, light echoes should be detected around a much broader list of objects than currently exists. To this end, an observational effort to put these ideas into practice is currently underway for the four classes of objects discussed in this work.

I offer my thanks to: Bruce Draine for making his dust scattering calculations publically available, and for helpful discussions; Peter Hauschildt and Ed Baron for generously providing synthetic Phoenix spectra; Christian Knigge, Raghvendra Sahai, Roger Chevalier and Arlin Crotts for useful discussions and feedback; and the referee, Bill Sparks, for his critical reading of this manuscript, thoughtful and insightful feedback, and for bringing echoes around RS Pup to my attention. This paper made use of publically-available data from the AAVSO International Database, SUSPECT supernova spectrum archive, General Catalog of Variable Stars, and the Catalog and Atlas of Cataclysmic Variables. *Synphot* is developed and maintained by the Science Software Group at STScI. This work was generously supported by Arlin Crotts and STScI grants GO 8806, 8872, 9111, 9328 & 9343, and NSF AST 02 06048.

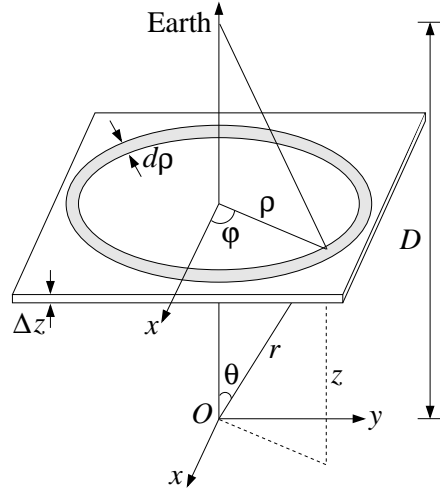


Fig. 1.— Echo geometry used in this paper. Note that the distances are not to scale, and D is much larger than z . Adapted from Xu et al. (1994).

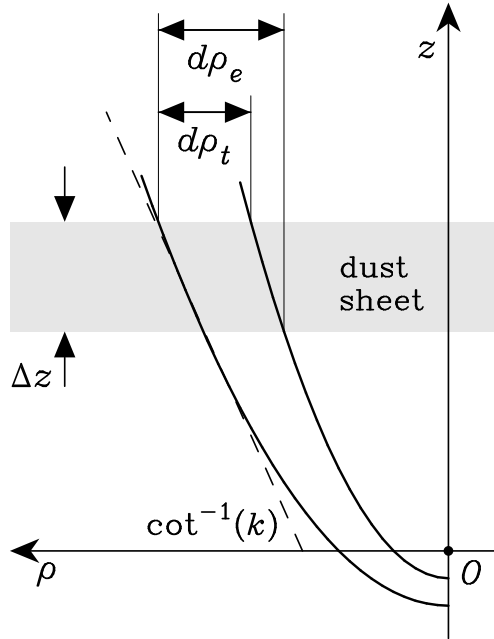


Fig. 2.— Schematic showing the contribution of dust thickness and finite light-pulse duration on the observed width of a light echo. Adapted from Xu et al. (1995).

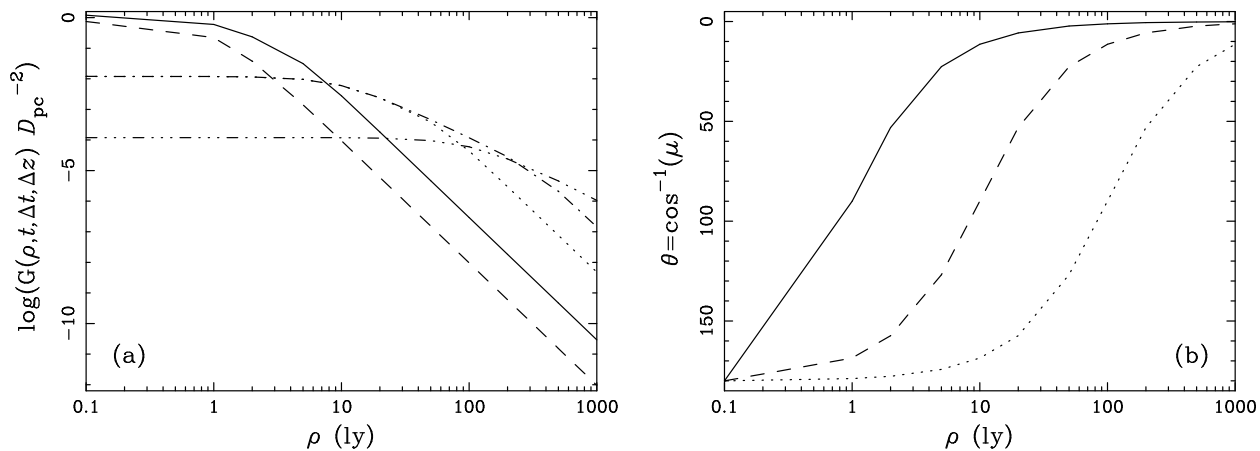


Fig. 3.— Geometric factors in B_{SC} [eq. (7)]. (a) The geometric function $G(\rho, t, \tau, \Delta z)$ [eq. (12)] for input $(t, \tau, \Delta z)$ as follows: solid line (1 y, 3 d, 0.1 ly); dashed (1 y, 0.25 y, 0.1 ly); dot-dashed (10 y, 3 d, 5 ly); dotted (10 y, 0.25 y, 5 ly); dot-dot-dot-dashed (1000 y, 0.25 y, 25 ly). (b) $\theta(\rho, t)$ for $t=1$ y (solid line), 10 y (dashed line), 1000 y (dotted line).

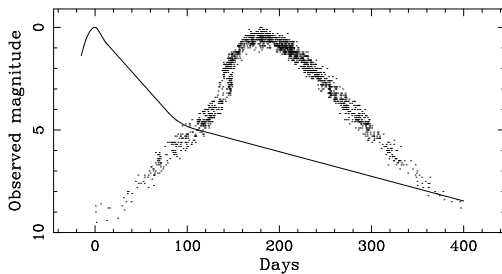


Fig. 4.— Light curves for variable objects. Solid curve – mean light curve below maximum light in B for Type II-L SNe. Points – V light curve (shifted by -5 mags) for the Mira χ Cyg (from AAVSO International Database). The maxima can be well represented by semi-logarithmic parabolae (§3.3.1).

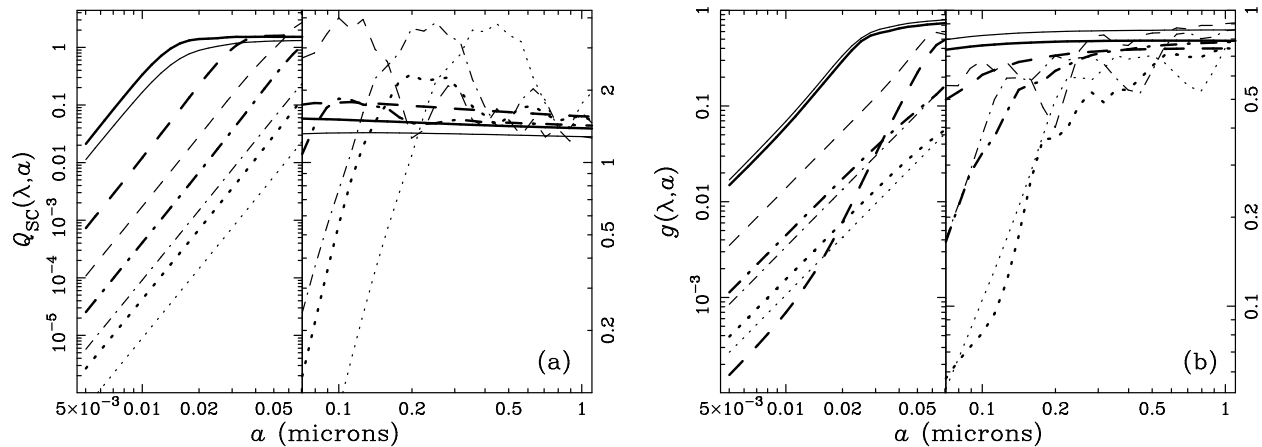


Fig. 5.— (a) Scattering efficiency $Q_{SC}(\lambda, a)$ and (b) forward scattering $g(\lambda, a)$ for carbonaceous (heavy lines) and silicate (thin lines) grains. Solid lines show values for 1000\AA , dashed lines for 2500\AA , dot-dashed lines for 5000\AA , and dotted lines for 8900\AA . For clarity, values for the smallest grain sizes are shown at different scales, as noted on the ordinates and abscissae.

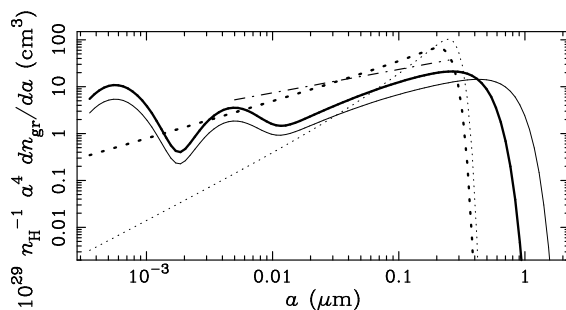


Fig. 6.— Dust grain density distributions for carbonaceous (solid lines) and silicate (dotted lines) dust. Thick lines are for the $R_V = 3.1$, $b_C = 6 \times 10^{-5}$ model, and thin lines are for the $R_V = 5.5$, $b_C = 3 \times 10^{-5}$ model of WD01. For clarity, and to allow the reader to estimate the mass present in each size range, data are plotted in units of $a^4 dn_{gr}/da$. The dot-dashed line shows the corresponding density distribution from MRN.

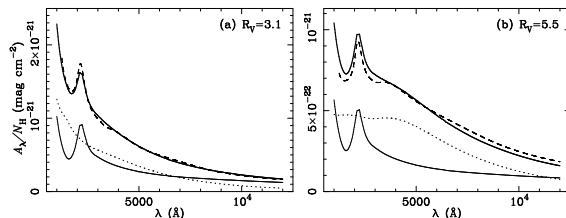


Fig. 7.— Extinction curves as functions of R_V . The lower curves show the extinction per unit hydrogen column density for carbonaceous (solid line) and silicate (dotted line) dust as integrated from equation (18) (§2.6). The thick upper line is the total extinction, i.e. the sum of these two components. The thin upper line is the extinction from Cardelli et al. (1989), normalized so that $A_V = 5.02 \times 10^{-22}$ for $R_V = 3.1$, and $A_V = 4.77 \times 10^{-22}$ for $R_V = 5.5$.

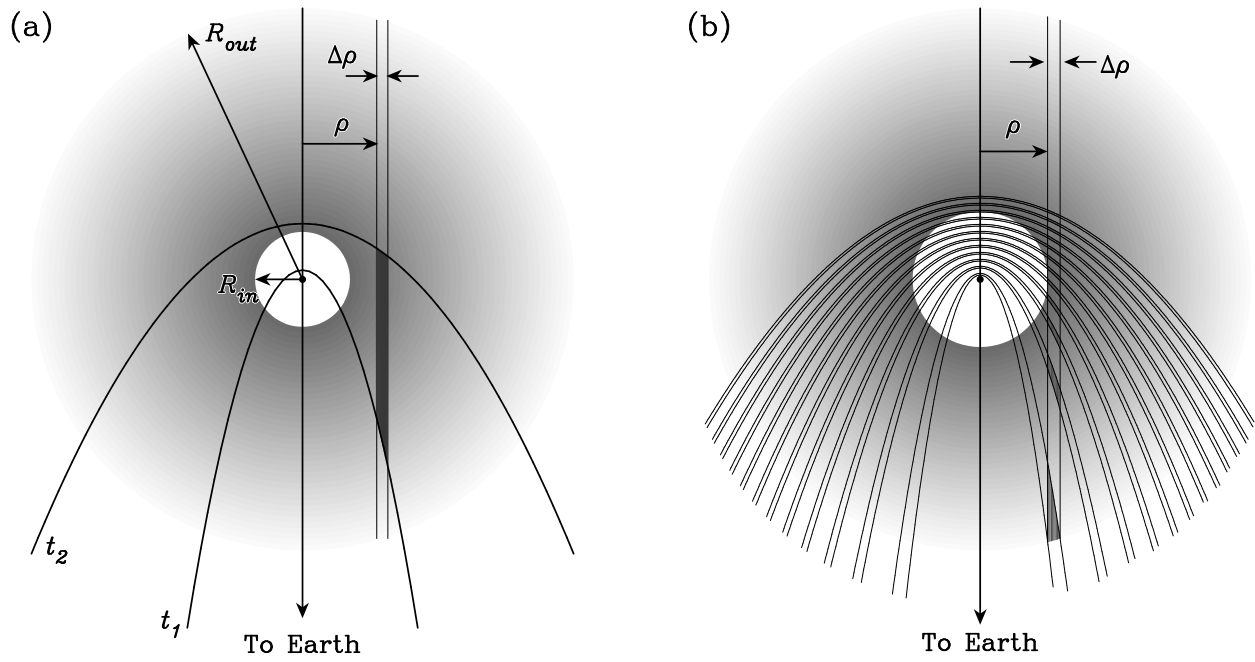


Fig. 8.— Schematic diagrams of light echoes within CSEs. (a) A thick-echo regime where only one echo passes through the CSE at a time (typical of Miras). (b) A thin-echo regime where many echoes fill the CSE at once (typical of Cepheids). See text (§§2.7, 3.3.4 and 3.3.5).

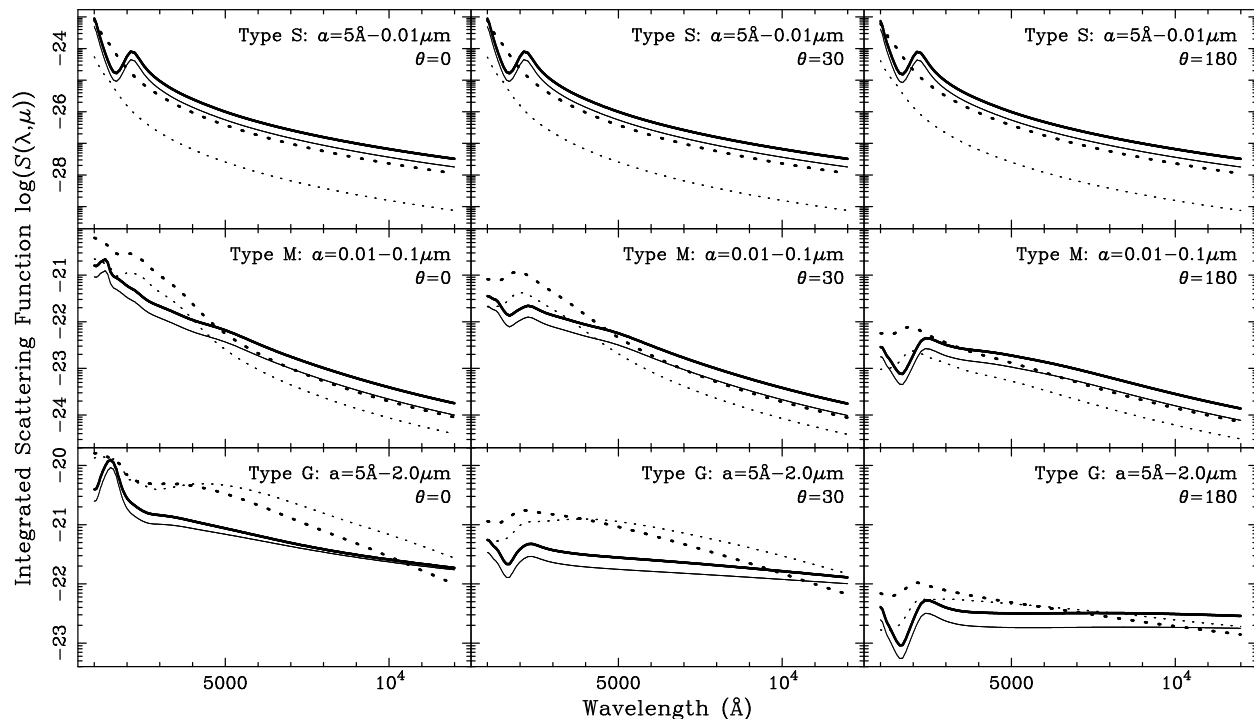


Fig. 9.— Integrated scattering function $S(\lambda, \mu)$ [eq. (8)]. Line thickness designates the density distribution model: thick lines are for $R_V = 3.1$, and thin lines for $R_V = 5.5$ (§2.4). Line style designates dust composition: solid lines show carbonaceous dust, and dotted lines show silicates. The first row has been calculated for type S dust (§3.1), the second row for type M and the third row for type G. The first column is calculated for $\theta = 0^\circ$, the second for $\theta = 30^\circ$, and the third for $\theta = 180^\circ$.

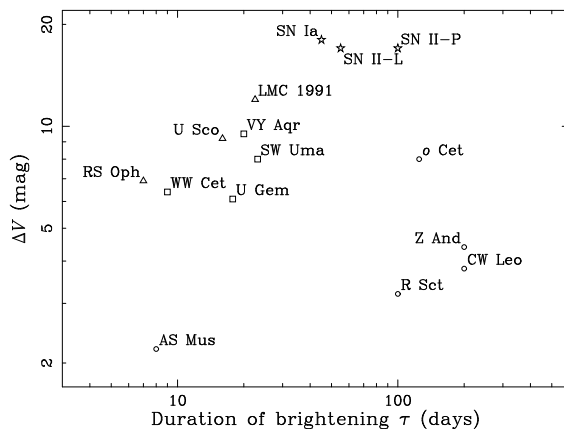


Fig. 10.— Duration of brightening τ versus change in brightness ΔV for the objects listed in Table 4. Supernovae are marked with stars, classical and recurrent novae with triangles, cataclysmic variables (dwarf and TOAD novae) with squares, and mass-losing giant stars with circles.

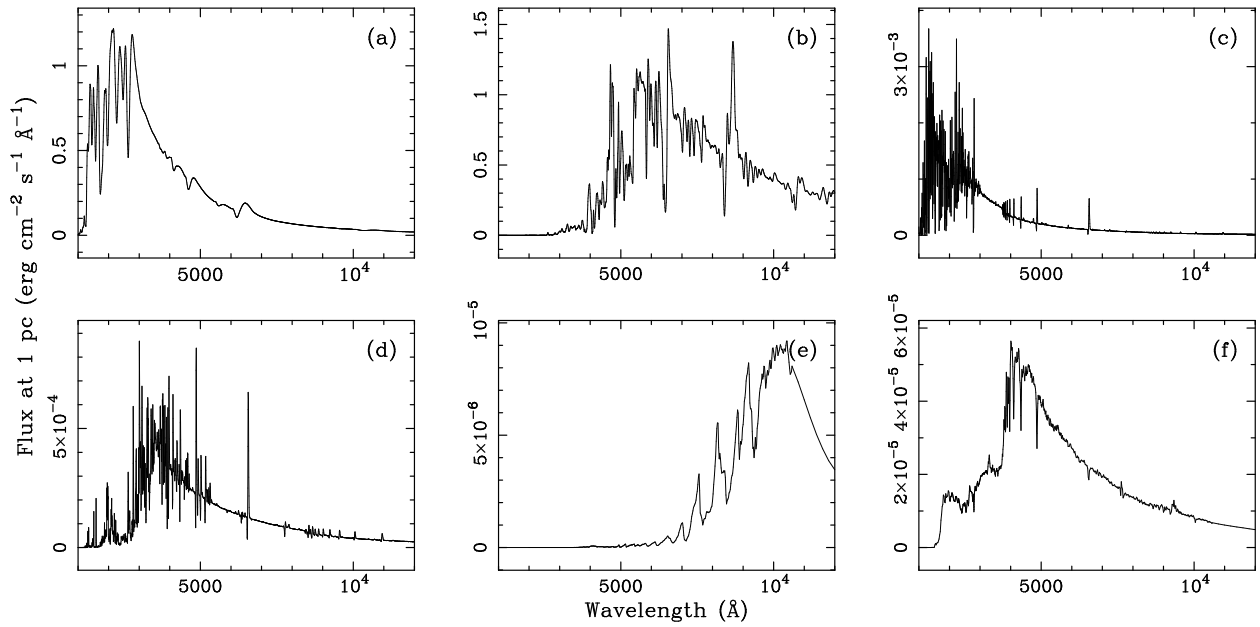


Fig. 11.— Spectra used in this work, with fluxes normalized to a distance of 1 pc. *Phoenix* synthetic spectra for (a) SN 1987A at day 1, and (b) at day 58, (c) a classical nova during the fireball stage, and (d) a classical nova during the constant luminosity phase; (e) the M7III star SW Vir (typical of Miras) from the BPGS catalog within *synphot*; (f) the F0IV star ξ Ser from the BPGS catalog, normalized to the F6Ib spectrum of HD 8992 (typical of a bright Cepheid).

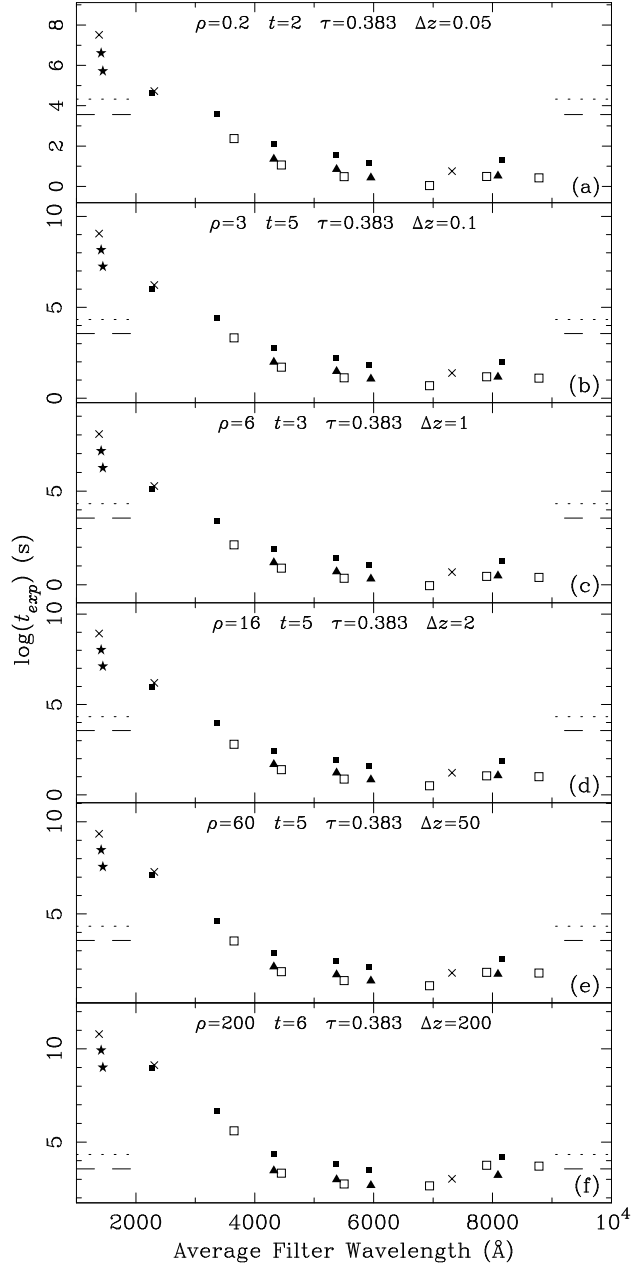


Fig. 12.— Exposure times necessary to image an echo with $S/N = 3$ (per pixel) for a supernova. Filters are plotted at their central wavelengths (Table 2), with STIS filters denoted by crosses, Johnson/Cousins by open squares, and ACS filters by filled symbols, with stars for the SBC, squares for the HRC, and triangles for the WFC. Geometric parameters are listed at the top of each panel and correspond to those in Table 5. The dust is assumed to follow a type-G (Galactic) size distribution. Dashed and dotted lines denote “reasonable” exposure-time upper limits for *HST* and ground-based observations, respectively. UV filter ($\langle \lambda \rangle < 2600 \text{\AA}$) exposure times are for the UV burst spectrum, all others are for the optical peak spectrum.

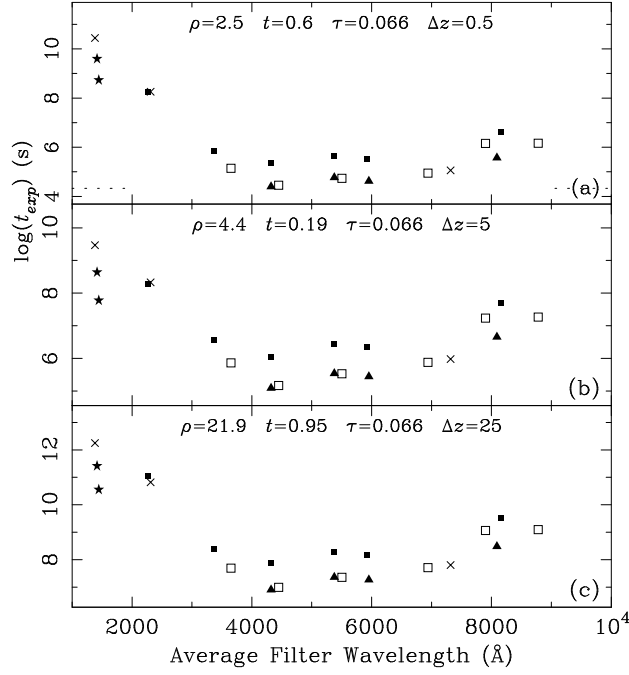


Fig. 13.— Same as Figure 12 but for a classical nova. As in Figure 12, UV filter ($\langle \lambda \rangle < 2600\text{\AA}$) exposure times are for the UV burst spectrum, all others are for the optical peak spectrum.

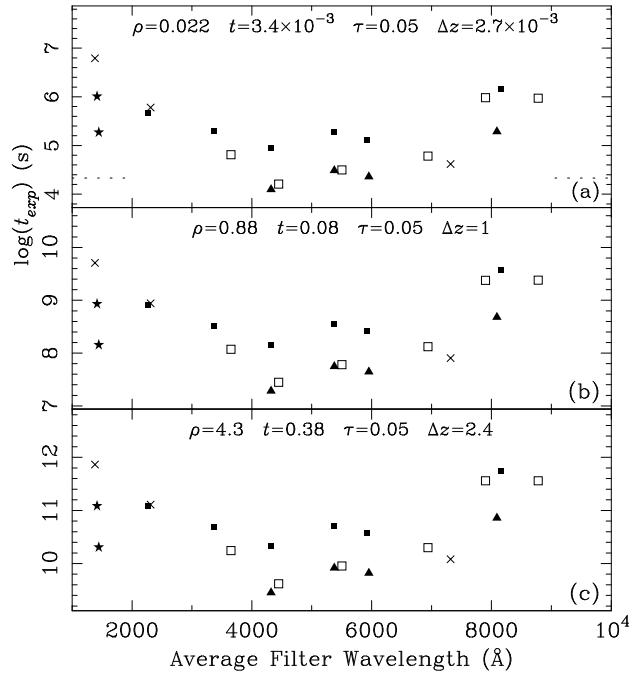


Fig. 14.— Same as Figure 12 but for a TOAD nova. There is no distinction between UV and optical exposure times.

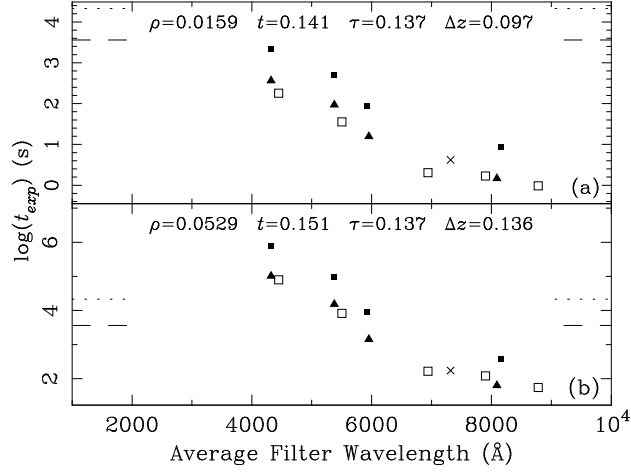


Fig. 15.— Same as Figure 12 but for a Mira, assuming the thick-echo approximation (§2.7). UV exposure times are all longer than the ordinate limits.

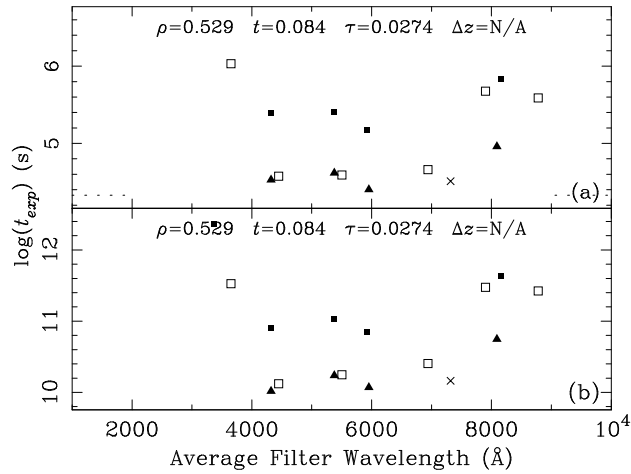


Fig. 16.— Same as Figure 12 but for a Cepheid, assuming the thin-echo approximation (§2.7). UV exposure times are all longer than the ordinate limits. (a) is for a mass-loss rate of $10^{-6} M_{\odot} \text{ yr}^{-1}$, and (b) is for $10^{-9} M_{\odot} \text{ yr}^{-1}$.

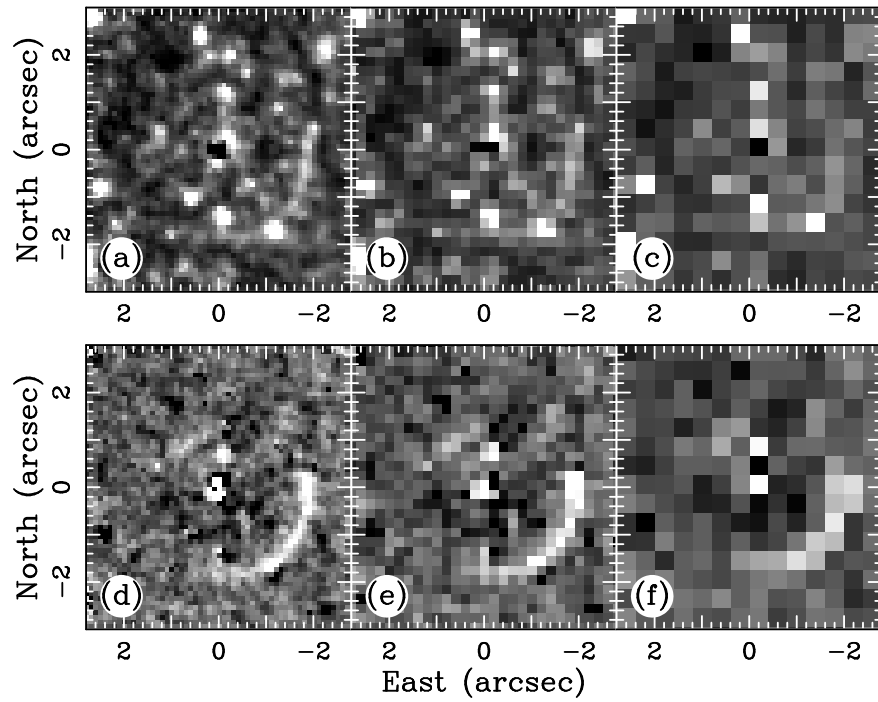


Fig. 17.— F555W images of echoes around SN 1993J from SC02. The SN (at the origin) has been PSF subtracted but residuals remain. Panel (a) shows the direct image on WF4 taken in 2001, with resolution degraded by two in (b) and again in (c). Panel (d) shows the PSF-matched difference between 2001 and 1995, and difference images between the input images degraded by two in (e) and again by two in (f).

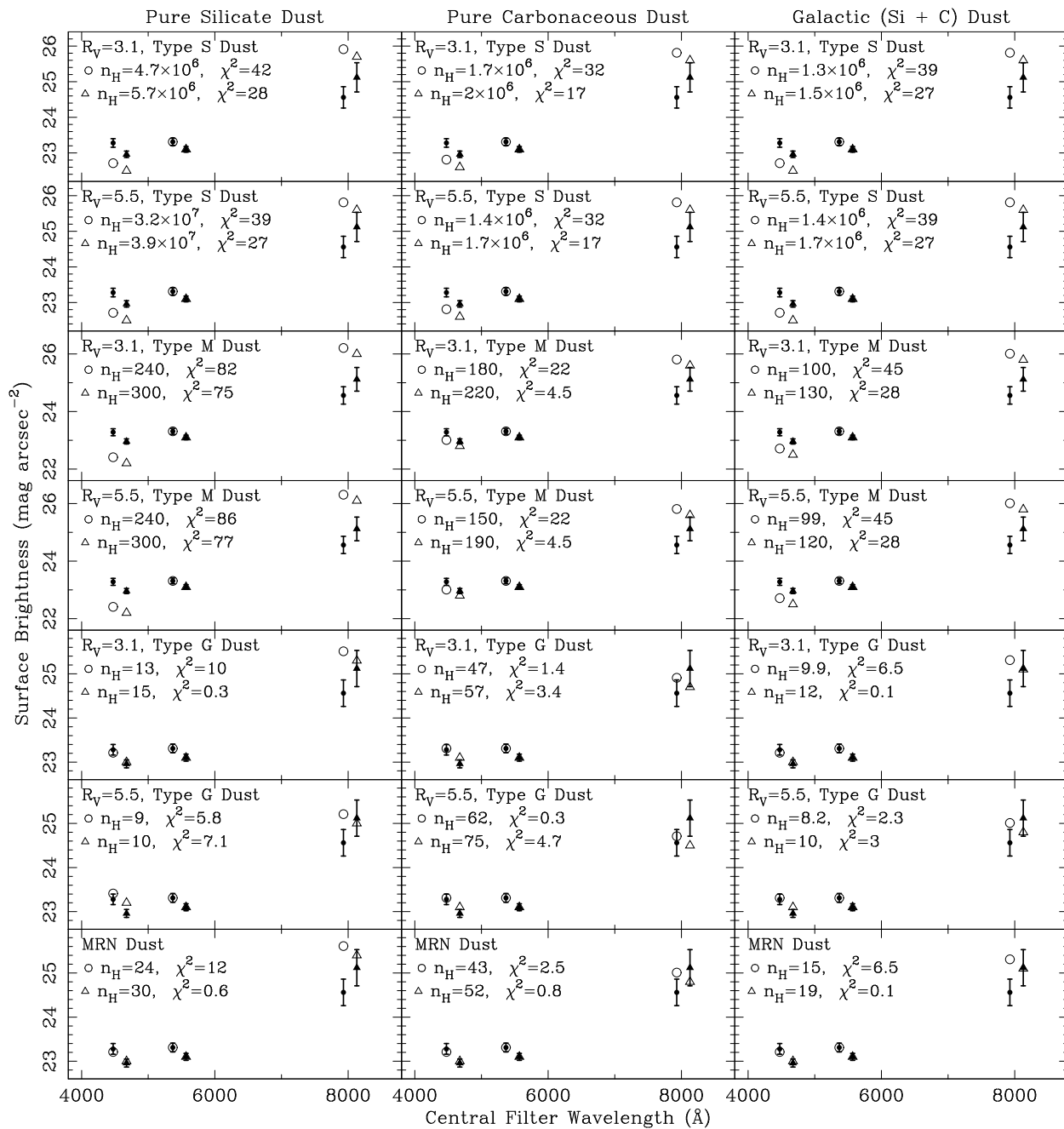


Fig. 18.— Model predictions for the brightness of echoes around SN 1993J for compositions as noted at the top of each column. Solid points are surface brightnesses as measured by SC02 for the SW770 echo, plotted about the central wavelengths of the corresponding WFPC2 filters (F450W, F555W, and F814W). Open points are the model predictions. Within each pair, the left point (circles) is for the echo near PA 220, and the right point (triangles) is for PA 270. Each model fit is scaled by n_H calculated to match the F555W datum. These values of n_H , as well as the χ^2 residuals and the grain-size distribution, are noted in each panel.

Table 1. Mean Widths of Supernova Light Curves

| SN Type | τ (days) | | | | | % of total flux included | | | |
|---------|---------------|----|----|-----|-----|--------------------------|-----|-----|-----|
| | 1 | 2 | 3 | 4 | 5 | 1,2 | 3 | 4 | 5 |
| Ia | 24 | 22 | 31 | 38 | 46 | 65% | 74% | 80% | 90% |
| II-P | 46 | 42 | 64 | 120 | 160 | 76% | 65% | 95% | 95% |
| II-L | 26 | 28 | 39 | 60 | 72 | 94% | 95% | 95% | 96% |

¹Effective width that Sparks (1994) measured starting at maximum light.

²Effective width that I measure starting at maximum light.

³Effective width that I measure using the entire light curve.

⁴Time for light curve to rise and fall by 2 mags.

⁵ $2t_2$ as measured starting from maximum light.

Table 2. Characteristics of Filters Used in This Work

| Sysytem | Filter | $\langle\lambda\rangle^a$ | $\Delta\lambda^b$ | T_{peak}^c | C_{sky}^d |
|---------|----------------------|---------------------------|-------------------|---------------------|----------------------|
| STIS | FUV MAMA | 1381.9 | 324.0 | 0.045 | 3.5×10^{-3} |
| STIS | NUV MAMA | 2309.5 | 1237. | 0.031 | 0.025 |
| STIS | F28X50LP | 7318.7 | 2684.9 | 0.124 | 0.01 |
| ACS WFC | F435W | 4321.9 | 698.7 | 0.372 | 0.028 |
| ACS WFC | F555W | 5375.9 | 847.5 | 0.375 | 0.055 |
| ACS WFC | F606W | 5953.6 | 1575. | 0.468 | 0.136 |
| ACS WFC | F814W | 8092.2 | 1541. | 0.439 | 0.104 |
| ACS HRC | F220W | 2265.6 | 442.1 | 0.051 | 10^{-4} |
| ACS HRC | F330W | 3366.2 | 410.7 | 0.105 | 6×10^{-4} |
| ACS HRC | F435W | 4321.2 | 728.5 | 0.223 | 4.3×10^{-3} |
| ACS HRC | F555W | 5369.6 | 841.4 | 0.239 | 9.9×10^{-3} |
| ACS HRC | F606W | 5920.1 | 1557. | 0.276 | 0.024 |
| ACS HRC | F814W | 8152.3 | 1651. | 0.223 | 0.016 |
| ACS SBC | F115LP | 1415.0 | 354.5 | 0.0580 | 0.024 |
| ACS SBC | F125LP | 1445.3 | 334.1 | 0.0529 | 0.0027 |
| Johnson | <i>U</i> | 3673.0 | 478.0 | 0.050 | 0.17 |
| Johnson | <i>B</i> | 4519.2 | 894.3 | 0.058 | 0.13 |
| Johnson | <i>V</i> | 5556.6 | 836.3 | 0.115 | 0.26 |
| Johnson | <i>R</i> | 6784.6 | 1559. | 0.137 | 0.98 |
| Cousins | <i>I_C</i> | 7818.9 | 873.8 | 0.094 | 0.90 |
| Johnson | <i>I</i> | 8285.7 | 1464. | 0.076 | 0.86 |

^aAverage wavelength $\langle\lambda\rangle = \int T(\lambda)\lambda d\lambda / \int T(\lambda)d\lambda$ in Å.

^bFWHM of filter in Å.

^cPeak throughput of filter and telescope.

^dSky background in $\text{e}^- \text{s}^{-1} \text{pix}^{-1}$, for “typical” conditions defined in §2.5.

Table 3. Characteristics of Detectors Used in This Work

| Instrument | Platescale arcsec pix ⁻¹ | Read Noise e ⁻ | Gain e ⁻ DN ⁻¹ | Dark Current e ⁻ s ⁻¹ pix ⁻¹ |
|------------------------|--|------------------------------|---|--|
| STIS FUV MAMA | 0.0246 | 0. | 1. | 3×10^{-5} |
| STIS NUV MAMA | 0.0246 | 0. | 1. | 2×10^{-3} |
| STIS CCD | 0.0507 | 4.2 | 1. | 2.5×10^{-3} |
| ACS WFC | 0.05 | 5.0 | 1.0 | 2×10^{-3} |
| ACS HRC | 0.027 | 4.7 | 2.2 | 2.5×10^{-3} |
| ACS SBC | 0.032 | 0.0 | 1.0 | 1.2×10^{-5} |
| SITE f/15 ^a | 0.15 | 5.4 | 3.3 | $4. \times 10^{-3}$ |

^aGround-based observations on a generic f/15 2.4m ground-based telescope. See §2.5

Table 4. Variable Objects with $\Delta V \gtrsim 2$ mag

| Class | Example | ΔV (mag) | W (days) ^a | Reference |
|------------------|------------|------------------|-----------------------|-----------|
| Supernovae | | | | |
| SN Ia | ... | 18 | 40 | 1 |
| SN II-P | ... | 17 | 140 | 1 |
| SN II-L | ... | 17 | 70 | 1 |
| CVs | | | | |
| CI Nova | LMC 1991 | 12 | 20–25 | 2 |
| U Sco | U Sco | 9.2 | 16 | 3 |
| RS Oph | RS Oph | 6.9 | 6–8 | 3 |
| U Gem | U Gem | 6.1 | 17.8 | 3,4 |
| Z Cam | WW Cet | 6.4 | 9 | 3,4 |
| SS Cyg | SS Cyg | 3.2 | 8 | 3,4 |
| SU Uma | SW Uma | 8. | 23.1 | 3,5 |
| WZ Sge | VY Aqr | 9.5 | 20 | 3,5 |
| Symbiotic | Z And | 4.4 | 200 | 6 |
| Pulsating Giants | | | | |
| Mira/LPV | χ Cyg | 8. | 100 | 6 |
| RV Tauri | R Sct | 3.2 | 100 | 6 |
| Post-AGB | CW Leo | 3.8 | 220 | 6 |
| Cepheid | AS Mus | 2.2 | 8 | 6 |
| Eruptive Stars | | | | |
| S Doradus | η Car | 9 | 2020 | 6 |

^bDuration of outburst or τ .

References. — (1) composite light curves from Doggett & Branch (1985); (2) Schwarz et al. (2001); (3) Catalog and Atlas of Cataclysmic Variables (<http://icarus.stsci.edu/~downes/cvcat/index.html>); (4) Ak, Ozkan, & Mattei (2002); (5) Howell et al. (1995); (6) General Catalog of Variable Stars (<http://www.sai.msu.su/groups/cluster/gcvs/gcvs/>)

Table 5. Adopted Geometric Parameters

| Echo ^a | ρ (ly) | t (y) | τ^b (y) | Δz (ly) | z (ly) | θ ($^\circ$) | $\Delta\rho$ (ly) | D_{max}^c (kpc) |
|-------------------|----------------|------------|-----------------|--------------------|-------------|--------------------------|----------------------|----------------------|
| Supernovae | | | | | | | | |
| C | 0.2 | 2. | 0.003/0.383 | 0.05 | -0.99 | 168 | 2. | 25. |
| C | 3.0 | 5. | 0.003/0.383 | 0.10 | -1.6 | 118 | 0.47 | 380 |
| B | 6.0 | 3. | 0.003/0.383 | 1.0 | 4.5 | 53. | 0.69 | 760 |
| B | 16. | 5. | 0.003/0.383 | 2.0 | 23.1 | 35. | 0.92 | 2.0×10^3 |
| I | 60. | 5. | 0.003/0.383 | 50. | 358 | 10. | 4.8 | 7.6×10^3 |
| I | 200. | 6. | 0.003/0.383 | 200. | 3330 | 3.42 | 8.8 | $25. \times 10^3$ |
| Novae | | | | | | | | |
| C | 2.5 | 0.6 | 0.003/0.066 | 0.5 | 4.9 | 27. | 0.19 | 320 |
| I | 4.4 | 0.19 | 0.003/0.066 | 5.0 | 50. | 5. | 0.80 | 560 |
| I | 21.9 | 0.95 | 0.003/0.066 | 25.0 | 250. | 5. | 1.3 | 2.7×10^4 |
| TOAD Novae | | | | | | | | |
| C | 0.022 | 0.0034 | 0.05 | 0.0027 | 0.069 | 30. | 0.17 | 0.3 |
| B | 0.88 | 0.08 | 0.05 | 1. | 5. | 10. | 0.29 | 110 |
| I | 4.3 | 0.38 | 0.05 | 2.4 | 24. | 10. | 0.30 | 10^3 |
| Miras | | | | | | | | |
| C | 0.0159 | 0.141 | 0.137 | 0.097 | 0.027 | 30. | 0.002 | 2.0 |
| C | 0.0529 | 0.151 | 0.137 | 0.136 | 0.092 | 30. | 0.002 | 6.7 |
| Cepheids | | | | | | | | |
| C | 0.264 | 0.0977 | 0.0274 | N/A ^d | N/A | N/A | 0.05 | 33. |

^aC: Circumstellar Echo; B: Contact Discontinuity; I: Interstellar Echo

^bIf two values listed, the first is for the UV burst, the second for the optical maximum. For Giant Stars, this column lists $\Delta\rho$ in ly.

^cMaximum distance of source assuming a minimum echo/source separation of $0''.5$ using the *HST*. See text (§3.4).

^dFor the thin-echo case, the sum of all echoes within the CSE is measured, thus Δz , z , and θ are not applicable.

REFERENCES

- Ak, T., Ozkan, M. T., & Mattei, J. A. 2002, *A&A*, 389, 478
- Argyle, E. 1974, *Icarus*, 21, 199
- Band, D. L. & Hartmann, D. H. 1992, *ApJ*, 386, 299
- Barbon, R., Benetti, S., Cappellaro, E., Patat, F., Turatto, M., & Iijima, T. 1995, *A&AS*, 110, 513
- Benson, P.J., et al. 1994, *AJ*, 107, 1453
- Bode, M. F. & Evans, A. 1985, *A&A*, 151, 452
- Bode, M. F. & Evans, A. 1989, *Classical Novae* (Chichester: Wiley)
- Boffi, F. R., Sparks, W. B., & Macchetto, F. D. 1999, *A&AS*, 138, 253
- Bond, H. E. et al., *Nature*, in press
- Braun, E. & Milgrom, M. 1989, *ApJ*, 337, 644
- Bromley, B. C. 1992, *PASP*, 104, 1049
- Cannizzo, J. K. & Mattei, J. A. 1998, *ApJ*, 505, 344
- Cappellaro, E. et al. 2001, *ApJ*, 549, L215
- Cardelli, J. A., Clayton, G. C. & Mathis, J. S. 1989, *ApJ*, 345, 245
- Chevalier, R. A. 1974, *ApJ*, 188, 501
- Chevalier, R. A. 1986, *ApJ*, 308, 225
- Chugai, N. N. 1992, *Soviet Astronomy*, 36, 63
- Crotts, A. P. S. 1992, *ApJ*, 399, L43
- Crotts, A. P. S. & Heathcote, S. R. 2000, *ApJ*, 528, 426
- Crotts, A. P. S. & Kunkel, W. E. 1991, *ApJ*, 366, L73
- Crotts, A. P. S., Kunkel, W. E. & Heathcote, S. R. 1995, *ApJ*, 438, 724
- Couderc, P. 1939, *Ann. d'Ap.*, 2, 271
- Deasy, H. P. 1988, *MNRAS*, 231, 673
- de Diego, J. A., Dultzin-Hacyan, D., Benitez, E., & Thompson, K. L. 1998, *A&A*, 330, 419
- Di Carlo, E. et al. 2002, *ApJ*, 573, 144
- Doggett, J. B. & Branch, D. 1985, *AJ*, 90, 2303
- Draine, B. T. & Lee, H. M. 1984, *ApJ*, 285, 89 (Erratum: 318, 485)
- Emmering, R. T. & Chevalier, R. A. 1988, *AJ*, 95, 152

- Emmering, R. T. & Chevalier, R. A. 1989, *ApJ*, 338, 388
- Filippenko, A. V., Barth, A. J., Bower, G. C., Ho, L. C., Stringfellow, G. S., Goodrich, R. W., & Porter, A. C. 1995, *AJ*, 110, 2261
- Freedman, W.L., et al. 1994, *ApJ*, 427
- Gaidos, E. J. 1994, *Icarus*, 109, 382
- Gehrz, R. D. 1988, *ARA&A*, 26, 377
- Habing, H. J. 1996, *A&A Rev.*, 7, 97
- Havlen, R. J. 1972, *A&A*, 16, 252
- Heney, L. C. & Greenstein, J. L. 1941, *ApJ*, 93, 70
- Harrison, T. E., McNamara, B. J., Szkody, P., McArthur, B. E., Benedict, G. F., Klemola, A. R., & Gilliland, R. L. 1999, *ApJ*, 515, L93
- Howell, S. B., 2000, “Handbook of CCD Astronomy,” (New York: Cambridge University Press)
- Howell, S. B., Szkody, P., & Cannizzo, J. K. 1995, *ApJ*, 439, 337
- Jorissen, A. & Knapp, G. R. 1998, *A&AS*, 129, 363
- Justtanont, K., Skinner, C. J., & Tielens, A. G. G. M. 1994, *ApJ*, 435, 852
- Kastner, J. H., Weintraub, D. A., Zuckerman, B., Becklin, E. E., McLean, I., & Gatley, I. 1992, *ApJ*, 398, 552
- Kastner, J. H., Soker, N., Rappaport, S. A. 2000, *ASP Conf. Ser.* 199: Asymmetrical Planetary Nebulae II: From Origins to Microstructures (San Francisco: ASP)
- Katz, J. I. 1987, *A&A*, 182, L19
- Knigge, C. & Drew, J. E. 1987, *ApJ*, 486, 445
- Knigge, C. & Livio, M. 1998, *MNRAS*, 297, 1079
- Lamers, H. J. G. L. M. & Cassinelli, J. P. 1999, *Introduction to stellar winds* (New York: Cambridge University Press)
- Laor, A. & Draine, B. T. 1993, *ApJ*, 402, 441
- Lawrence, S. S., Sugerman, B. E., Bouchet, P., Crofts, A. P. S., Uglesich, R. R., & Heathcote, S. R. 2000, *ApJ*, 537, 123
- Leitherer, C. et al., 2001, “STIS Instrument Handbook,” Version 5.1, (Baltimore: STScI)
- Lewis, J. R. et al. 1994, *MNRAS*, 266, L27
- Li, A. & Draine, B. T. 2001, *ApJ*, 554, 778
- Lira, P. et al. 1998, *AJ*, 115, 234

- Liu, J.-F., Bregman, J. N. & Seitzer, P. 2002, *ApJ*, 582, 919
- Lynden-Bell, D. 1969, *Nature*, 223, 690
- Mackey, W. R. 1987, *ApJ*, 315, 251
- Maslov, I. A. 2000, *Astronomy Letters*, 26, 428
- Mathis, J. S., Rimpl, W., & Nordsieck, K. H. 1977, *ApJ*, 217, 425 (MRN)
- Mayes, A. J., Evans, A., & Bode, M. F. 1985, *A&A*, 142, 48
- McKee, C. F. & Ostriker, J. P. 1977, *ApJ*, 218, 148
- Milgrom, M. 1987, *A&A*, 182, L21
- Munari, U. et al. 2002, *A&A*, 389, L51
- Pavlovsky, C., et al. 2002, *ACS Instrument Handbook*, Version 3.0, (Baltimore: STScI).
- Perryman, M. A. C. et al. 1997, *A&A*, 323, L49
- Polidan, R. S. & Holberg, J. B. 1984, *Nature*, 309, 528
- Prabhu, T. P. et al. 1995, *A&A*, 295, 403
- Press, W.H., et al. 1992, *Numerical Recipes in Fortran*, 2nd ed. (Cambridge: University Press)
- Reichart, D. E. 2001, *ApJ*, 554, 643
- Richmond M. W., et al. 1994, *AJ*, 107, 1022
- Ritchey, G. W. 1901, *ApJ*, 14, 293
- Roscherr, B. & Schaefer, B. E. 2000, *ApJ*, 532, 415
- Schaefer, B. E. 1987a, *ApJ*, 323, L51
- Schaefer, B. E. 1987b, *ApJ*, 323, L47
- Schaefer, B. E. 1988, *ApJ*, 327, 347
- Schmidt, B. P., Kirshner, R. P., Leibundgut, B., Wells, L. A., Porter, A. C., Ruiz-Lapuente, P., Challis, P., & Filippenko, A. V. 1994, *ApJ*, 434, L19
- Schwarz, G. J., Shore, S. N., Starrfield, S., Hauschildt, P. H., Della Valle, M., & Baron, E. 2001, *MNRAS*, 320, 103
- Seaquist, E. R., Bode, M. F., Frail, D. A., Roberts, J. A., Evans, A., & Albinson, J. S. 1989, *ApJ*, 344, 805
- Sholomitskii, G. B. 1997, *Ap&SS*, 252, 177
- Sparks, W. B. 1994, *ApJ*, 433, 19
- Sparks, W. B. 1996, *ApJ*, 470, 195

- Sparks, W. B. 1997, in “The Extragalactic Distance Scale,” STScI Symposium Series 10, Eds. Livio, M., Donahue, M., & Panagia, N. (Cambridge: Cambridge University Press), p. 281
- Sparks, W. B., Macchetto, F., Panagia, N., Boffi, F. R., Branch, D., Hazen, M. L., & della Valle, M. 1999, *ApJ*, 523, 585
- Stecher, T. P. 1965, *ApJ*, 142, 1683
- Stecher, T. P. & Donn, B. 1965, *ApJ*, 142, 1681
- Swenson, J. W. 1948, Ph.D. Thesis,
- Sugerman, B. E. K. & Crofts, A. P. S. 2002, *ApJ*, 581, L97
- Sugerman, B. E. K., Lawrence, S. S., Crofts, A. P. S., Bouchet, P., Heathcote, S. R., 2002, *ApJ*, 572, 209
- Sugerman, B., Sahai, R., & Hinkle, K. 1996, *IAU Symp. 170: CO: Twenty-Five Years of Millimeter-Wave Spectroscopy*, 170, 108P
- Tomaney, A., & Crofts, A. P. S. 1996, *AJ*, 112, 2872
- Tweedy, R. W. 1995, *ApJ*, 438, 917
- Uglesich, R., Mirabal, N., Sugerman, B., & Crofts, A. 1999, *BAAS*, 195, 132.06
- Uglesich, R. R. 2002, Ph.D.T
- van de Hulst, H. C. 1957, “Light Scattering by Small Particles,” (New York: John Wiley & Sons)
- van den Bergh, S. 1965a, *AJ*, 70, 667
- van den Bergh, S. 1965b, *PASP*, 77, 269
- van den Bergh, S. 1966, *PASP*, 78, 74
- van den Bergh, S. 1977, *PASP*, 89, 637
- Vassiliadis, E. & Wood, P. R. 1993, *ApJ*, 413, 641
- Vitello, P. & Shlosman, I. 1993, *ApJ*, 410, 815
- Walker, A. 1987, *NOAO Newsletter*, 10, 16
- Warner, B. 1995, “Cataclysmic Variable Stars,” *Cambridge Astrophysics Series*, (New York: Cambridge University Press)
- Weingartner, J. C. & Draine, B. T. 2001, *ApJ*, 548, 296 (WD01)
- Wright, E. L. 1980, *ApJ*, 242, L23
- Xu, J., Crofts, A. P. S. & Kunkel, W. E. 1994, *ApJ*, 435, 274
- Xu, J., Crofts, A. P. S. & Kunkel, W. E. 1995, *ApJ*, 451, 806 (Erratum: 463, 391)
- Xu, J. & Crofts, A.P.S. 1999, *ApJ*, 511, 262